Table of Contents

Introduction

There exists a number of design requirements necessitating incorporation of various cutouts to the walls, webs and panels of airplane structures. These allow for cables, hydraulic lines and wiring to be laid, provide inspectability, etc. If a cutout is to be made in a structural member, i.e. a frame, rib, bulkhead, an alternate load path must be provided, otherwise stress concentration must be countered with padding or other types of structural reinforcement. Furthermore, such a design is susceptible to fatigue cracking arising from stress increase due to the abovementioned effects.

For large-scale cutouts, such as doors and transparencies, two design approaches are employed. First, the corner radii are maximized to prevent premature cracking of the cutout corners. Second, the cutout perimeter is reinforced with bulkheads, sills, straps and pad-ups of the skin.

Cold formed sheet metal solid structures are often used in the fuselage design, be it frames or floor beams (both exhibiting numerous cutouts in the web). It is prohibitively expensive to manufacture a conventional thickness pad-up at the cutout perimeter. The use of satellite fasteners is also not desired. A viable solution to this problem is cold forming a flanged hole. This design, however, is not without its limitations.

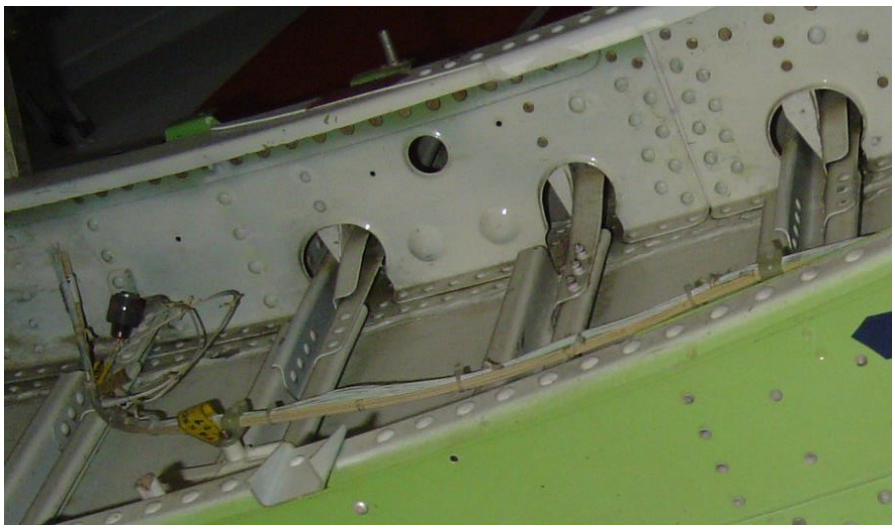

Figure 1 – Cutout in a Formed Section Frame

Another example of cutouts in a structural element occurs in a rib of the wing. While the ribs, like other wing structures are not made of sheet metal, rather, they are generally milled from a plate, they are somewhat heavily loaded by:

1) aerodynamic load transferred from the adjacent wing skin;
2) vertical shear from wing spars;
3) shear from mounted equipment, i.e. flaps, engines, landing gear;
4) fuel slosh.

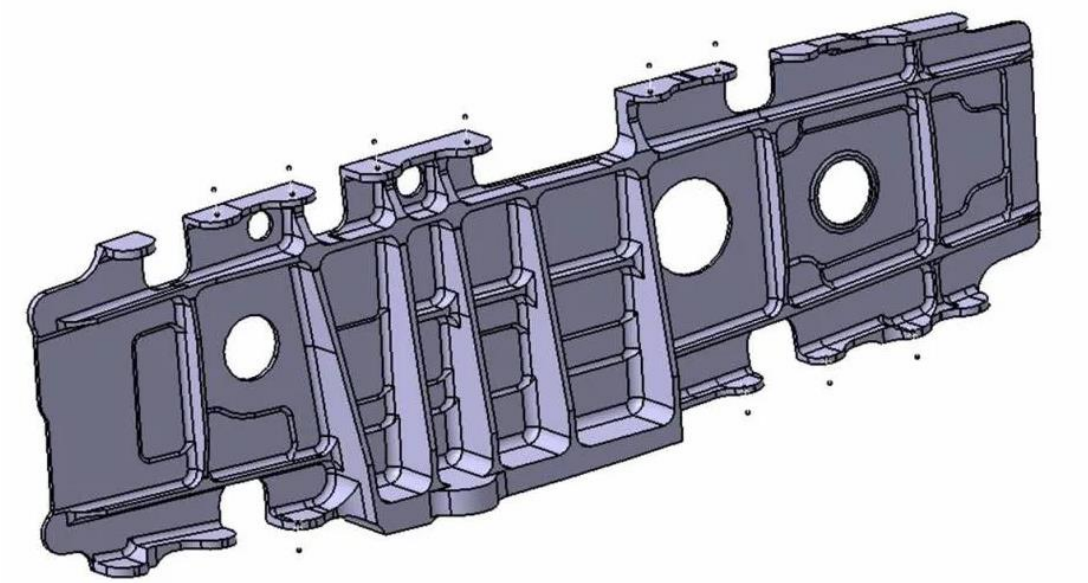

Figure 2 – Cutouts in a Machined Rib

Figure 3 – Cutouts in Typical Floor Beams

Chapter 1. Formulation of the Problem.

1.1 The Necessity of Research

As the market for commercial transport category aircraft is highly competitive, the regulations considering airworthiness and operational safety are ever tightening. Development and further research into existing methods of increasing the strength of the airframe is necessary for continuously maintaining a competitive advantage.

Development and operation of modern aircraft puts a high demand on engineering and design, involves computed aided solutions for manufacturing, design and other fields of engineering.

Maintaining the competitive advantage on the world market therefore requires constant innovation, scientific research and development to satisfy the need for strength, safety, efficiency and cost during all stages of the product life cycle.

Cutouts in structural members is a widespread solution to the ever-present need for accessibility, inspectability and maintenance, cable routing and manufacturability of certain airplane structures. A single structure may exhibit few to several dozens of these cutouts, each of which requires special considerations and dedicated testing to determine their effects on the structures' ultimate capability.

As such, research into hole (cutout) reinforcement, its effects on shear buckling in particular, presents a multitude of viable problems.

1.2 The Task at Hand

First, it is set forth that introduction of cutouts plays key role in decreasing the material capability of the affected structure. As stated previously, instability and stress concentration at the cutout are responsible for the loss of capability. For thin walled structures, the onset of buckling usually precedes material yield. This is helpful, since elastic buckling is significantly less complicated than plastic buckling, which governs ultimate capability of plates. The task is to classify and quantify the abovementioned effects.

Second, it is necessary to quantify the effect of cutout reinforcement and approximate weight savings resulting from employing such techniques.

Tests designed to assess the theoretical results and methods are generally subdivided into three categories:

1) Full-scale tests, involving as-built structures in true operational conditions;

2) Sub-scale tests, involving separate assemblies, installations, joints, in approximated operational conditions;

3) Lab tests, involving test specimen and requiring special loading setups, mimicking the idealized theoretical model.

Research into shear instability of plates has a fundamental drawback in that, the real-life structures usually never exhibit pure shear loading.

The following requirements apply when analyzing the shear instability of plates in laboratory conditions:

1) The rigidity of the setup and its components is required to be several orders of magnitude more than the rigidity of the specimen, in order to ensure the deformation of the setup does not influence the behavior of the model and skew analysis results;

2) It is not acceptable to allow for torsion or bending of the plate as it approaches and reaches the buckling point;

3) The boundary conditions must approximate the theoretically modelled constraints as closely as possible.

4) Normal stresses in the plate must be negligible, while shear stresses bust be as uniform as possible;

5) The setup should ideally be easy to manufacture and versatile, allowing for testing of variously sized specimen.

A simple setup satisfying all of the abovementioned requirements is proposed. It is depicted in Figures 4 and 5 below. The setup is designed to be assembled without need for special manufacturing equipment and can be made from readily available stock. This setup allows for testing of various shapes and sizes of specimen.

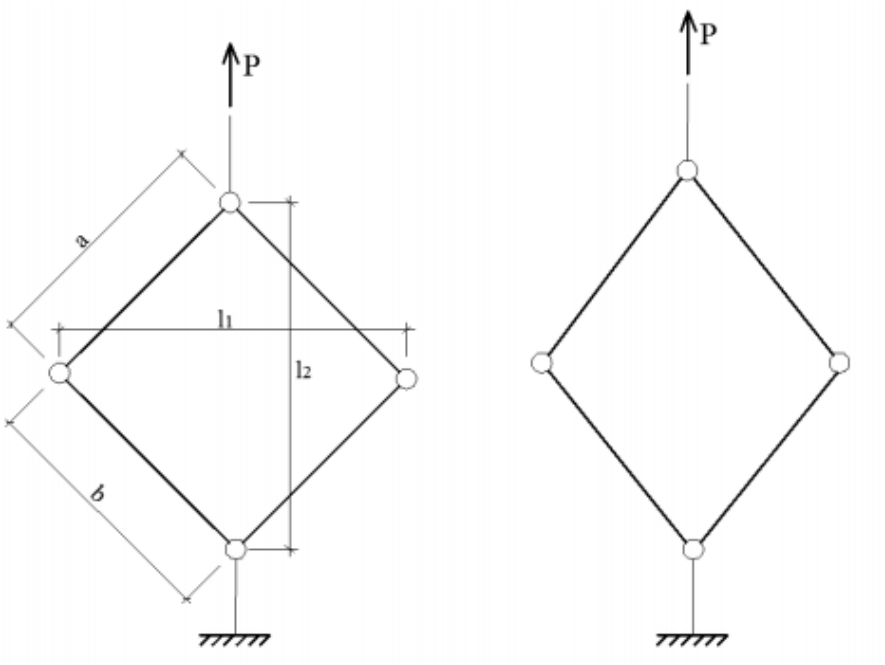

Figure 4 – Test Setup Principal Scheme

The perimeter is comprised of either cold-rolled or extruded L-sections, which provide ample rigidity against bending and out of plane deflections. The plate being tested is then clamped to the testing setup with removable fasteners. Sufficient clamping force is required to ensure the plate does not slip.

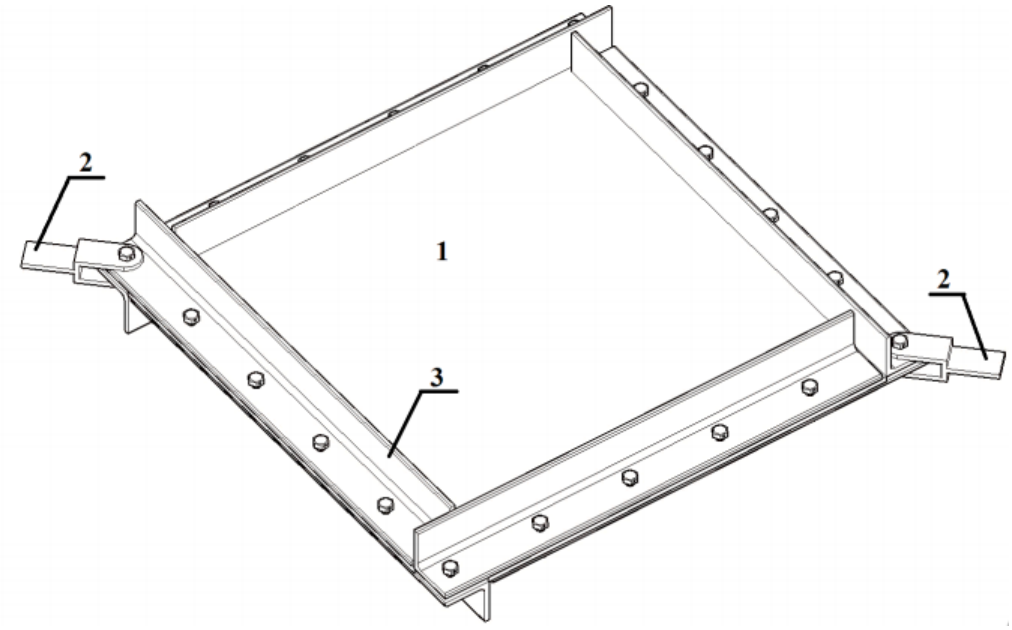

Figure 5 – General View of the Test Setup

On the Figure 5 above:

1 – the plate being tested;

2 – load application attachments;

3 – boundary clamping beams.

As far as the material of the test specimen, it is acceptable to use Plexiglas for several reasons, including the fact that it has lower Young's modulus and ultimate strength, which allows for less load being applied and a lighter setup. Note: the thermal expansion properties of Plexiglass differ severely from those of aluminum and steel. Care must be taken to ensure the thermal equilibrium is maintained at all stages of testing not to compromise the accuracy of the results.

It is important to perform validation of the test results, as well as to compare the results to those obtained with Finite Element Analysis methods. This allows to further confirm the validity and provides further insight into the behavior of the specimen being tested.

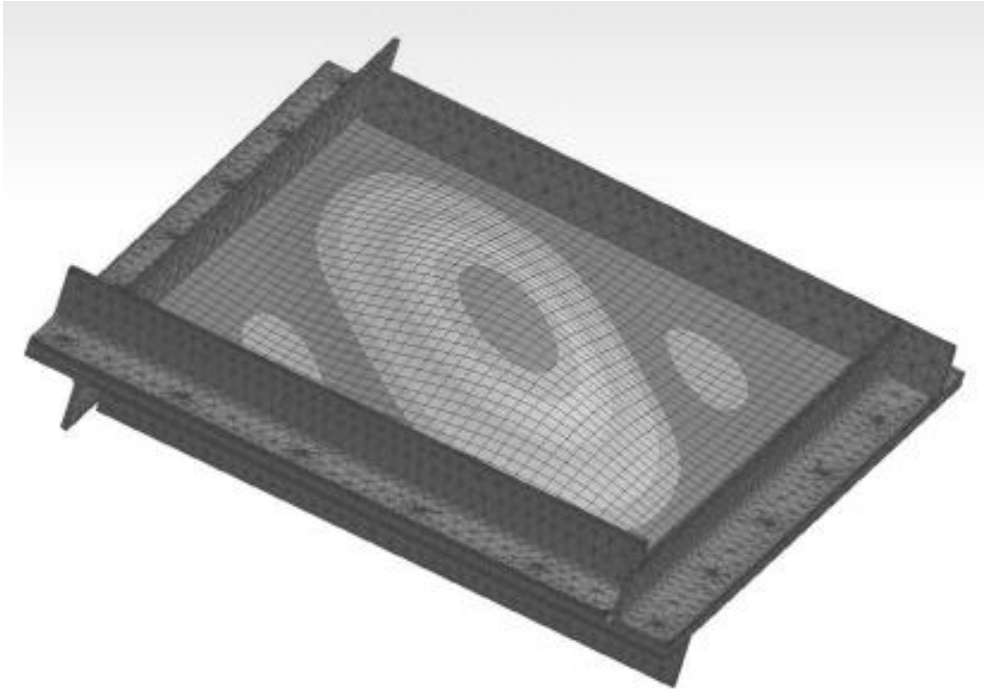

Figure 6 – FEM Analysis Results

As seen from Figure 6, the Finite Element Model analysis provides adequate representation of the buckling mode observed during laboratory testing of physical specimen.

One important aspect to note is the lack of twisting or displacement of unsupported nodes. If such a condition occurs, the plate becomes deformed, which may cause the buckling modes to differ significantly from what is expected.

The setup involving bolts is fundamentally flawed in that corner fastener locations become overly loaded. A special precaution must be observed when assembling the described setup in order to ensure the fastener is capable of sustaining the required load. Both bearing and fastener shear are to be considered in general.

1.3 Conclusion

Analysis of the results obtained shows leads to the following conclusions:

1) The proposed setup for testing the shear buckling of flat rectangular plates follows all applicable requirements and allows for obtaining accurate results.

2) The setup performs the best with rectangular plates where sides are equal in length, with relatively weak materials.

3) The test setup provides a variable fixity of the edges of the plate, which should generally be assumed as clamped support. This is a limitation, since it is not possible to analyze simply supported or free boundary conditions, or a mix of boundary conditions.

4) The setup requires special precautions to be observed for safe operation and obtaining accurate results.

Objective

The objective of this research is gaining insight into the behavior of reinforced cutouts in conditions of pure shear loading, the effects of reinforcement on stability and stress distribution. This will allow for improved design, weight savings and therefore increased profitability of the airplane in operation.

The objective is achieved with the aid of Finite Element Modeling (FEM) as implemented in MSC Patran and MSC Nastran applications.

Chapter 2. Computer Aided Analysis of Reinforced Cutouts in Plates

2.1 Finite Element Modeling (FEM)

Finite Element Modeling was first established when the need for solving complex elastic structural analysis tasks arisen in civil, naval and aerospace engineering.

In the early twentieth century, it was first speculated that there is a possibility for modeling complex structures as a sum of simpler elements. In shipbuilding and construction of aircraft, these elements were the stringers, frames, stanchions, skin panels, etc. Hrennikoff (1941) first proposed the lattice analogy for modeling membrane and plate bending of structures, which he later developed to include the lattice models for plate and shell buckling. Maney, Ostenfeld (1920) devised a method of solving for stress distribution in a hinged frame with an array of linear algebraic equations. These methods sadly did not get widely implemented due to lack of computational capabilities.

Early development of the Finite Element Modeling also got attention of Courant (1942). The consensus between him and his colleagues was in the concept of dividing the continuous region into smaller subregions, often called elements.

In his works, Hrennikoff proposed to use an orthogonal grid for subdividing the region. Meanwhile, Courant advocated for triangular elements, which better correspond to the solution of the partial differential equations (PDE) of the second order. These equations arise when solving the problem of torsion of the cylinder. Courant's contribution was evolutionary, drawing on a large body of earlier results for PDEs developed by Rayleigh, Ritz, and Galerkin.

The finite element method obtained its real impetus in the 1960s and 1970s by the developments of Argyris with co-workers at the University of Stuttgart, Clough with co-workers at UC Berkeley, Zienkiewicz with co-workers Hinton, Irons and others at Swansea University, Ciarlet at the University of Paris and

Gallagher with co-workers at Cornell University. Further impetus was provided in these years by available open source finite element software programs. NASA sponsored the original version of Nastran, and UC Berkeley made the finite element program SAP IV widely available. In Norway the ship classification society Det Norske Veritas developed Sesam in 1969 for use in analysis of ships. A rigorous mathematical basis to the finite element method was provided in 1973 with the publication by Strang and Fix. The method has since been generalized for the numerical modeling of physical systems in a wide variety of engineering disciplines, e.g., electromagnetism, heat transfer, and fluid dynamics.

A finite element method is characterized by a variational formulation, a discretization strategy, one or more solution algorithms and post-processing procedures.

Examples of variational formulation are the Galerkin method, the discontinuous Galerkin method, mixed methods, etc.

A discretization strategy is understood to mean a clearly defined set of procedures that cover (a) the creation of finite element meshes, (b) the definition of basis function on reference elements (also called shape functions) and (c) the mapping of reference elements onto the elements of the mesh. Each discretization strategy has certain advantages and disadvantages.

There are various numerical solution algorithms that can be classified into two broad categories; direct and iterative solvers. These algorithms are designed to exploit the sparsity of matrices that depend on the choices of variational formulation and discretization strategy.

P_1 is a one-dimensional problem:

$$P_1: \quad \begin{cases} u''(x) = f(x) \; in \; (0,1), \\ u(0) = u(1) = 0, \end{cases} \tag{1.1.1}$$

where f is given, u is an unknown function of x, and u'' is the second derivative of u with respect to x.

P_2 is a two-dimensional problem:

$$P_1: \quad \begin{cases} u_{xx}(x,y) + u_{yy}(x,y) = f(x,y) \ \ in \ \ \Omega, \\ u = 0 \qquad\qquad\qquad\qquad\qquad on \ \ \partial\Omega \end{cases} \tag{1.1.2}$$

where Ω is a connected open region in the (x, y) plane whose boundary $\partial\Omega$ is nice (e.g., a smooth manifold or a polygon), and u_{xx} and u_{yy} denote the second derivatives with respect to x and y, respectively.

The problem P_1 can be solved directly by computing antiderivatives. However, this method of solving the boundary value problem (BVP) works only when there is one spatial dimension and does not generalize to higher-dimensional problems or to problems like $u + u'' = f$. For this reason, we will develop the finite element method for P_1 and outline its generalization to P_2.

The first step is to convert P_1 and P_2 into their equivalent weak formulations. If u solves P_1, then for any smooth function v that satisfies the displacement boundary conditions, i.e. $v = 0$ at $x = 0$ and $x = 1$, we have

$$\int_0^1 f(x)v(x)dx = \int_0^1 u''(x)v(x)dx \tag{1.1.3}$$

Conversely, if u with $u(0) = u(1) = 0$ satisfies (1.1.3) for every smooth function $v(x)$ then one may show that this u will solve P_1. The proof is easier for twice continuously differentiable u (mean value theorem) but may be proved in a distributional sense as well.

We define a new operator or map $\phi(u, v)$ by using integration by parts on the right-hand-side of (1.1.3):

$$\begin{aligned}&\int_0^1 f(x)v(x)dx = \int_0^1 u''(x)v(x)dx = \\ &= u'(x)v(x)\Big|_0^1 - \int_0^1 u'(x)v'(x)dx = -\int_0^1 u'(x)v'(x)dx = -\phi(u,v)\end{aligned} \tag{1.1.4}$$

where we have used the assumption that $v(0) = v(1) = 0$.

If we integrate by parts using a form of Green's identities, we see that if u solves P_2, then we may define $\phi(u, v)$ for any v by

$$\int_\Omega f\, v\, ds = -\int_\Omega \nabla u \cdot \nabla v\, ds = -\phi(u,v) \tag{1.1.5}$$

where ∇ denotes the gradient and $\cdot$ denotes the dot product in the two-dimensional plane. Once more ϕ can be turned into an inner product on a suitable space $H_0^1(\Omega)$ of once differentiable functions of Ω that are zero on $\partial\Omega$. We have also assumed that $v \in H_0^1(\Omega)$. Existence and uniqueness of the solution can also be shown.

We can loosely think of $H_0^1(0,1)$ to be the absolutely continuous functions of (0, 1) that are zero at $x = 0$ and $x = 1$. Such functions are (weakly) once differentiable and it turns out that the symmetric bilinear map ϕ then defines an inner product which turns $H_0^1(0,1)$ into a Hilbert space (a detailed proof is nontrivial). On the other hand, the left-hand-side $\int_0^1 f(x)v(x)dx$ is also an inner product, this time on $L^2(0, 1)$. An application of the Riesz representation theorem for Hilbert spaces shows that there is a unique u solving (1.1.4) and therefore P_1.

This solution is a-priori only a member of $H_0^1(0,1)$ but using elliptic regularity, will be smooth if *f* is.

P_1 and P_2 are ready to be discretized which leads to a common sub-problem P_3. The basic idea is to replace the infinite-dimensional linear problem:

Find $u \in H_0^1$ such that

$\forall v \in H_0^1,\ -\phi(u,v) = \int f v$

with a finite-dimensional version:

Find $u \in V$ such that

$\forall v \in V,\ -\phi(u,v) = \int f v$

where *V* is a finite-dimensional subspace of H_0^1. There are many possible choices for *V* (one possibility leads to the spectral method). However, for the finite element method we take *V* to be a space of piecewise polynomial functions.

We take the interval (0, 1), choose *n* values of *x* with

$0 = x_0 < x_1 < \cdots < x_n < x_{n+1} = 1$ and we define *V* by:

$$V = \{v : [0,1] \to \mathbb{R} : v \text{ is continuous}, v\big|_{[x_k, x_{k+1}]} \text{ is linear for } k = 0, \ldots, n, \text{ and } v(0) = v(1) = 0\}$$

where we define $x_0 = 0$ and $x_{n+1} = 1$. Observe that functions in *V* are not differentiable according to the elementary definition of calculus. Indeed, if $v \in V$ then the derivative is typically not defined at any $x = x_k, k = 1, \ldots, n$. However, the derivative exists at every other value of *x* and one can use this derivative for the purpose of integration by parts.

We need V to be a set of functions of Ω. The space V would consist of functions that are linear on each triangle of the chosen triangulation.

One hopes that as the underlying triangular mesh becomes finer and finer, the solution of the discrete problem P_3 will in some sense converge to the solution of the original boundary value problem P_2. To measure this mesh fineness, the triangulation is indexed by a real valued parameter $h > 0$ which one takes to be very small. This parameter will be related to the size of the largest or average triangle in the triangulation. As we refine the triangulation, the space of piecewise linear functions V must also change with h. For this reason, one often reads V_h instead of V in the literature. Since we do not perform such an analysis, we will not use this notation.

To complete the discretization, we must select a basis of V. In the one-dimensional case, for each control point x_k we will choose the piecewise linear function v_k in V whose value is 1 at x_k and zero at every $x_j, j \neq k$, i.e.,

$$v_k = \begin{cases} \dfrac{x - x_{k-1}}{x_k - x_{k-1}} & \text{if } x \in \left[x_{k-1}, x_k \right] \\ \dfrac{x_{k+1} - x}{x_{k+1} - x_k} & \text{if } x \in \left[x_k, x_{k+1} \right] \\ 0 & \text{otherwise} \end{cases} \tag{1.1.6}$$

For $k = 1,\ldots, n$ this basis is a shifted and scaled tent function. For the two-dimensional case, we choose again one basis function v_k per vertex x_k of the triangulation of the planar region Ω. The function v_k is the unique function of V whose value is 1 at x_k and zero at every $x_j, j \neq k$.

Depending on the author, the word "element" in "finite element method" refers either to the triangles in the domain, the piecewise linear basis function, or both. Finite element method is not restricted to triangles.

More advanced implementations (adaptive finite element methods) utilize a method to assess the quality of the results (based on error estimation theory) and modify the mesh during the solution aiming to achieve approximate solution within some bounds from the exact solution of the continuum problem. Mesh adaptivity may utilize various techniques, the most popular are:

1) moving nodes (r-adaptivity);
2) refining (and unrefining) elements (h-adaptivity);
3) changing order of base functions (p-adaptivity);
4) combinations of the above (hp-adaptivity).

Finite Element Modeling has several advantages:

1) By making the subregion to have relatively simple geometry, the basis functions end up being relatively simple and consistent.
2) By refining the sub-elements, the shape and form of Ω is approximated ever more accurate. This is vitally important for more complex geometries. It is possible to increase the density of sub-elements where a discontinuity or a large gradient in the solution is expected.
3) It is relatively easy to find the basis functions that satisfy the boundary conditions of a sub-region.
4) Since the basis functions are zero outside of the subregion, the computational requirements are reduced.
5) The basis functions do not overlap; therefore, it is possible to integrate over the entire region by adding the results of integration of each sub-region.
6) FEM is extremely versatile and allows for solving any non-linear problems with a wide variety of material properties.
7) FEM is highly programmable which allows for its application in many fields.

2.2 Finite Difference Method (FDM)

Finite-difference methods are discretizations used for solving differential equations by approximating them with difference equations where finite differences approximate the derivatives.

FDMs convert a linear ordinary differential equations (ODE) or non-linear partial differential equations (PDE) into a system of equations that can be solved by matrix algebra techniques. The reduction of the differential equation to a system of algebraic equations makes the problem of finding the solution ideally suited to modern computers, hence the widespread use of FDMs in modern numerical analysis.

Two FDMs are described below. First, the median derivative method, which is used for solving the static equilibrium equations in dynamic problems. This method is classified as direct integration method.

Equilibrium equation for a system of finite elements in motion is:

$$M\ddot{U} + C\dot{U} + KU = R \tag{1.2.1}$$

where M, C and K are the matrices of mass, dampening and rigidity respectively, R is the applied forces vector, U, $\dot{U}$ and $\ddot{U}$ are the vectors of translations, velocities and accelerations.

Direct numerical integration is based on several concepts. First, it is only necessary to satisfy the equilibrium equations at short discrete time intervals, and not continuously. Second, the change in U, $\dot{U}$ and $\ddot{U}$ may be accounted for, because they are assumed to be known, and the only thing left to be found is the solution to (1.2.1) within $t \in (0,T)$. The time period t is further subdivided into n equal sub-intervals Δt:

$$\Delta t = T / n \tag{1.2.2}$$

The Median Derivative Method assumes the following:

$$\ddot{U}_t = \frac{1}{\Delta t^2}\{U_{t-\Delta t} - 2U_t + U_{t+\Delta t}\} \tag{1.2.3}$$

Error resulting from (1.2.3) has an order of $(\triangle t)^2$, therefore, it is sufficient to use the following equations when solving for velocities:

$$\dot{U}_t = \frac{1}{2\Delta t}(-U_{t-\Delta t} + U_{t+\Delta t}) \tag{1.2.4}$$

Displacement at point of time $t+\triangle t$ is calculated with respect of (1.2.1) to *t*:

$$M\ddot{U}_t + C\dot{U}_t + KU_t = R_t \tag{1.2.5}$$

By substituting (1.2.3) and (1.2.4) into (1.2.5), we obtain an equation:

$$\left(\frac{1}{\Delta t^2}M + \frac{1}{2\Delta t}C\right)U_{t+\Delta t} = R_t \cdot \left(K - \frac{2}{\Delta t^2}M\right)U_t - \left(\frac{1}{\Delta t^2}M - \frac{1}{2\Delta t}C\right)U_{t+\Delta t} \tag{1.2.6}$$

which allows us to find $U_{t+\Delta t}$. Calculation of the displacement $U_{t+\Delta t}$ is based on equilibrium equations being satisfied at time *t* (1.2.5).

Another quirk of this method is that $U_{t+\Delta t}$ is obtained from U_t and $U_{t-\Delta t}$. Therefore, calculating the displacement requires a special pre-processing step.

Since U_0 ,$\dot{U}_0$ and $\ddot{U}_0$ are known (and if only U_0 ,$\dot{U}_0$ are known, then it is possible to find the rest by using (1.2.1)), then by using (1.2.3) and (1.2.4) the value of $U_{t-\Delta t}$ can easily be obtained:

$$U_{-\Delta t}^{(i)} = U_0^{(i)} - \Delta t \dot{U}_0^{(t)} + \frac{\Delta t^2}{2} \ddot{U}_0^{(i)} \tag{1.2.7}$$

where the upper index (*i*) denotes a corresponding vector element.

In case of absence of dampening, the equation (1.2.6) can be re-written as:

$$\left(\frac{1}{\Delta t^2} M \right) U_{t+\Delta t} = \hat{R}_t, \tag{1.2.8}$$

where

$$\hat{R}_t = R_t - \left(K - \frac{2}{\Delta t^2} M \right) U_t - \left(\frac{1}{\Delta t^2} M \right) U_{t-\Delta t} \tag{1.2.9}$$

The displacements are then obtained from the formula:

$$U_{t+\Delta t}^{(i)} = \hat{R}_t^{(i)} \left(\frac{\Delta t^2}{m_{il}} \right), \tag{1.2.10}$$

where $U_{t+\Delta t}^{(i)}$ and $\hat{R}_t^{(i)}$ are corresponding components of the vector $U_{t+\Delta t}$ and $\hat{R}_t$; m_{ij} is an element of the *M*.

It is not necessary to transform the rigidity matrix or the mass matrix to a triangular state, therefore, neither is it necessary to build *K* and *M* for the entire ensemble.

Since:

$$K = \sum_l K_l \; ; \; M = \sum_i M_i \tag{1.2.11}$$

Therefore, KU_t, $(2M/\Delta t^2)U_t$ and $(M/\Delta t^2)U_{t-\Delta t}$ in (1.2.9) need only be calculated on the element level by adding up each element's contribution in the loads vector. Thus, the following is true for $\hat{R}_t$:

$$\hat{R}_t = R_t - \sum_i (K_i U_t) - \sum_i \frac{1}{\Delta t^2} M_i (U_{t-\Delta t} - 2U_t) \tag{1.2.12}$$

where $K_i U_t$ and $M_i(U_{t-\Delta t} - 2U_t)$ are calculated with K_i and M_i in a compact formula.

2.3 Continuous medium

There are many known approaches for solving for the movement of a continuous medium. Some of the notable ones are: Lagrangian, Euleran and Lagrangian-Eulerian Formulation, the latter is often referred to as Lagrangian-Euleran Formulation (ALE).

Lagrangian formulation has limited applicability for problems with massive deformation of shape. It is generally not applicable where large deformations of the mesh are present.

Solving the ALE formulation sometimes involves displacing the nodes of the mesh so that the mesh warp is minimized. If material is flowing relative to the mesh, additional equations are used.

In a multi-material Euleran formulation, the medium is allowed to flow through the mesh, which is fixed in place. Furthermore, it is possible to have a mesh element which contains materials of several types. This is useful when solids are mixed with liquids, then, the Lagrangian approach is used for solids and Euleran for liquids. In general, this effect is called fluid-structure interaction.

Several equations make up the Lagrangian formulation, such as: conservation of mass, momentum, energy balance and a governing equation.

Mass conservation equation is:

$$\dot{\rho} + \rho \, div(v) = 0, \tag{1.3.1}$$

where ρ is the density and v the velocity.

Equation of conservation of momentum is:

$$\rho\ddot{x} = \rho g + div(\sigma), \tag{1.3.2}$$

where $\ddot{x}$ is acceleration, σ is the stress tensor, g is the free fall acceleration.

Equation of conservation of energy is:

$$\rho\dot{u} = \sigma : D + \rho r - \Delta \cdot q, \tag{1.3.3}$$

where $\dot{u}$ is the rate of change of the internal energy, D is the deformation rate, r *is* the intensity of the thermal source, q is the heat flow and : is the double scalar multiplication operator.

Spatial discretization of the equation of conservation of momentum involves going from (1.3.2) to solving the following:

$$\int_V \left(\rho\ddot{x} - \rho g - div(\sigma)\right) \cdot \Phi \, dv \tag{1.3.4}$$

with appropriate boundary conditions. By utilizing the procedures from FEM, solving equation (1.3.4) becomes solving the following:

$$M\ddot{d} = F_i + F_e \tag{1.3.5}$$

where $\ddot{d}$ is the vector of nodal velocities, F_i, F_e are vectors of internal and external forces respectively.

Spatial discretization of the equation of conservation of energy involves transitioning from equation (1.3.3) to solving

$$\int_V \left(\rho\ddot{u} - \sigma : D - \rho r + \Delta \cdot q\right) \cdot \phi \, dv \tag{1.3.6}$$

It is possible to transform the equation (1.3.6) to the following form:

$$M^{\theta}\dot{\theta} = F_t^{\theta} + F_e^{\theta} \tag{1.3.7}$$

where θ is the temperature, M^{θ} is the heat capacity matrix, $F_t^{\theta}, F_e^{\theta}$ are vectors of internal and external thermal loads respectively.

Vector of internal forces, included in equation (1.3.5) is defined by the third term of the expression integrated over:

$$\int_V div(\sigma)\cdot\Phi\, dv = \int_B (\sigma n)\cdot\Phi\, db - \int_V \sigma : (\Delta\Phi)\, dv \tag{1.3.8}$$

and it is equal to:

$$F_i = \int_V \sigma : (\Delta\Phi)\, dv \tag{1.3.9}$$

Vector F_i is obtained by adding up all internal forces for all elements included in the model. For each element, the vector of internal loads is defined by

$$f_i^e = \int_{V^e} B^T \bar{\sigma}\, dv, \tag{1.3.10}$$

where B is the derivative of the shape of the element, and $\bar{\sigma}$ comprises of six components of the stress tensor.

The vector of external forces F_e in equation (1.3.5) accounts for the distribution of the applied loads.

Nodal accelerations may be derived from (1.3.5) and are as follows:

$$\ddot{d} = M^{-1}\left(F_i + F_e\right) \tag{1.3.11}$$

By integrating over time with increments up to the second order of magnitude, accelerations, velocities and displacements are obtained:

$$\begin{aligned} \ddot{d}_n &= M^{-1}\left(F_i + F_e\right); \\ \dot{d}_{n+1/2} &= \dot{d}_{n-1/2}\,\ddot{d}_n \Delta t; \\ d_{n+1} &= d_n + \dot{d}_{n+1/2}\Delta t, \end{aligned} \tag{1.3.12}$$

The solution will be accurate, provided the time increment is:

$$\Delta t_{avg} = \frac{2}{\omega_{max}}, \tag{1.3.13}$$

where ω_{max} is the maximum natural frequency of the system.

It may often be cumbersome to determine ω_{max}, to cope with this, the frequency may be estimated:

$$\omega_{max} \approx \frac{2c}{\Delta x_{min}}, \tag{1.3.14}$$

where c is the speed of sound in the medium, Δx_{min} is the smallest element size.

The speed of deformation is defined by

$$\Delta\varepsilon = D\Delta t, \tag{1.3.15}$$

Euleran and ALE Formulations describe the movement of the medium through the mesh and therefore require additional laws of conservation. It should be noted that along with the medium flowing through the mesh, certain variables used to describe its prior states have to kept track of. Among these variables are density, temperature, strain, etc. These variables are referred to as historical variables. An example of a derivative of such a variable is shown below:

$$\dot{\varphi} = \varphi' + \Delta\varphi \cdot (v - \dot{x}), \tag{1.3.16}$$

where ϕ' is the derivative of the variable with respect to time in a static coordinate system, v is the velocity of the deformation of the mesh and $\dot{x}$ is the velocity of the material point.

In both Euleran and ALE formulations the nodes of the mesh do not follow the movement of the medium. Therefore, the energy conservation equation is altered:

$$\rho\dot{u} = \rho\nabla u \cdot (v - \dot{x}) + \sigma : D + \rho r - \nabla \cdot q \tag{1.3.17}$$

The equation that describes changes in historical variables is similar to equation (1.3.17). In this equation, $\dot{x} = \sigma : D = \sigma r = \nabla \cdot q,$ therefore $\dot{u} = \nabla u \cdot v.$ This leads to the conclusion that $u_x(t_0) = u_x(t_1)$.

The Lagrangian derivative with respect to time is calculated first, then with respect to the historical variable. The relative motion of the medium with respect to the mesh, and historical variables are made to correspond to nodes and elements of the static mesh.

The rate of flow of the medium defines the critical time step length:

$$\Delta t_{cr} \approx \min\left[\frac{\Delta x^e}{c}, \frac{2\Delta x^e}{v^e}\right], \tag{1.3.18}$$

where c is the speed of sound in the medium, Δx^e is the minimum typical mesh element size and v^e is the average number of nodes of an element.

Modifications of the mesh aimed at reducing distortions is called mesh rectification. In an Euleran formulation, after computing the Lagrangian step, the mesh returns to its initial configuration. ALE approach contains two options of mesh rectification after the Lagrangian step:

1) Direct method, which allows nodes to slide along pre-defined lines between adjacent nodes;
2) Iterative method of rectification.

Iterative solutions to mesh rectification seek out a new configuration of nodes which minimizes the distortion. After new node locations are obtained, historical variables are mapped over.

Chapter 3. Plate Buckling Analysis

As the plate element is subjected to various types of loading, such as direct compression, bending, shear or a combination thereof, the plate may buckle locally before the member becomes unstable or before the yield stress is reached. Such local buckling is characterized by out of plane deflection of the plate. Although buckling is often considered a sudden or discontinuous process, the inevitable presence of initial out of planeness results in a gradual growth of this displacement as the loading increases to the theoretical critical level.

The theoretical elastic buckling load is not on its own a basis for design. Where buckling of plates may be present, ultimate strength often exceeds the buckling limit. Unlike beam columns, buckled plates continue to provide structural capability due to post-buckling behavior. Therefore, additional load may be applied without structural damage. It may be argued that in an ideally designed structure, ultimate material capability should be reached during inelastic buckling. The presence of buckling, however, affects the redistribution of stresses within the member and therefore complicates the analysis of ultimate material capability.

An examination of the buckling behavior of a single plate supported along its edges is an essential preliminary step toward the understanding of local buckling behavior of plate assemblies. The buckling stresses are obtained from the concept of bifurcation of an initially perfect structure. In practice, the response of the structure is continuous, due to the inevitable presence of initial imperfections. Thus, the critical stress is best viewed as a useful index to the behavior, as slender plates can continue to carry additional loads well after initial buckling.

The analysis of the elastic critical stress for a rectangular plate simply supported along all edges and subjected to a uniform longitudinal compressive stress was presented in 1891 [8]. The elastic critical stress of a long plate segment is determined by the plate width-to-thickness ratio b / t, by the restraint conditions

along the longitudinal boundaries, and by the elastic material properties (elastic modulus, E, and Poisson's ratio v). The elastic critical stress σ_c is expressed as follows:

$$\sigma_c = k\frac{\pi^2 E}{12(1-\nu^2)(b/t)^2} \tag{2.1.1}$$

in which k is the plate buckling coefficient determined by a theoretical critical load analysis and is a function of both the plate geometry and boundary conditions illustrated below.

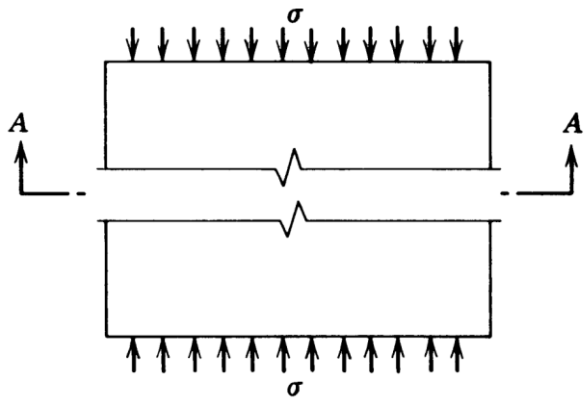

Figure 7 – Plate Loaded in Compression

Case	Edge Support	k
1	Both edges simply supported	4.00
2	One simply supported, other fixed	5.42
3	Both edges fixed	6.97
4	One simply supported, other free	0.43
5	One edge fixed, other free	1.28

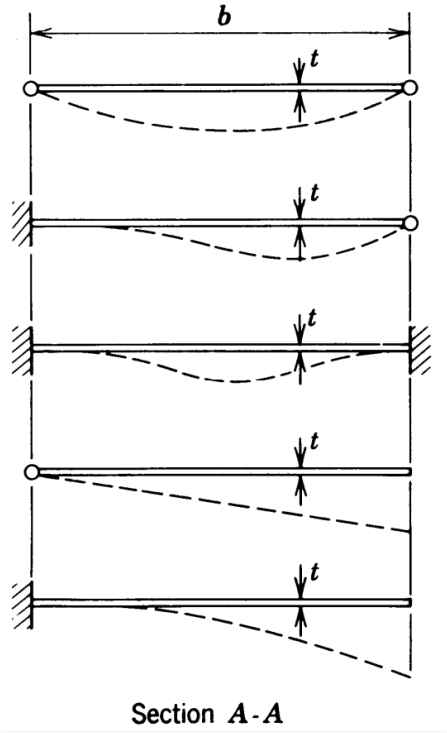

When a plate element is relatively short in the direction of the compressive stress there may exist an influence in the elastic buckling stress since the buckled halfwaves which take integer values are forced into a finite length plate.

The value of k varies as a function of normalized plate length; the variation is a function of the plate boundary conditions and the loading. Full analytical solutions for k as a function of the aspect ratio a / b may be found in Timoshenko and Gere [1], Allen and Bulson [9] and others. When a plate element is very short in the direction of the compressive stress (i.e. a / b << 1), the critical stress may be conservatively estimated by assuming that a unit width of plate behaves like a column.

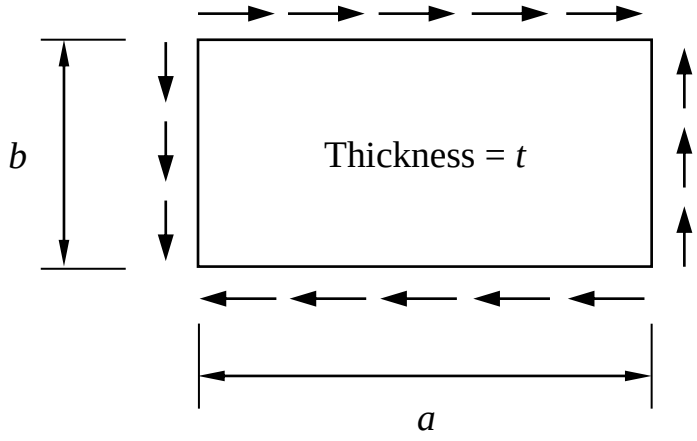

Figure 8 – Plate Loaded in Pure Shear

3.1 Shear Buckling of Plates

When a plate is subjected to edge shear stresses as shown in Figure 8, it is said to be in a state of pure shear. The critical shear buckling stress can be obtained by substituting σ_c and k in (2.1.1) for f_{sc} and k_s, in which k_s is the buckling coefficient for shear buckling stress. Critical stress coefficients, k_s, for plates subjected to pure shear have been evaluated for three conditions of edge support.

These relationships are plotted with the side *b*, as used in (2.1.1), always assumed to be shorter than side a. Thus, α is always greater than 1 and by plotting k_s in terms of 1 / α, the complete range of k_s can be shown and the magnitude of k_s remains manageable for small values of α.

The equation (2.1.1) can now be re-written as

$$Fs_{cr} = k_s \frac{\pi^2 E}{12(1-\nu^2)(b/t)^2} \tag{2.1.2}$$

Solutions developed by Timoshenko [2], Bergmann and Reissner [10], and Seydel [11] are approximated the following equations:

$$k_s = \begin{cases} 4.00 + 5.34/\alpha^2 & for\ \alpha \le 1 \\ 5.34 + 4.00/\alpha^2 & for\ \alpha \ge 1 \end{cases} \tag{2.1.3}$$

In 1924, Southwell and Skan obtained k_s = 8.98 for the case of the infinitely long rectangular plate with clamped edges. For the finite-length rectangular plate with clamped edges, Moheit [12] obtained

$$k_s = \begin{cases} 5.60 + 8.98/\alpha^2 & for\ \alpha \le 1 \\ 8.98 + 5.60/\alpha^2 & for\ \alpha \ge 1 \end{cases} \tag{2.1.4}$$

Sometimes a plate is clamped on two opposite edges and simply supported on the other two edges. A solution for this problem has been given by Iguchi [13] for the general case, and by Leggett [14] for the case of the square plate. Cook and Rockey [15] later obtained solutions considering the antisymmetric buckling mode which was not considered by Iguchi. The expressions below were obtained

by fitting a polynomial equation to the Cook and Rockey results. For long edges clamped, the equations are

$$k_s = \begin{cases} 8.98/\alpha^2 + 5.61 - 1.99\cdot\alpha & for\ \alpha \le 1 \\ 8.98 + 5.61/\alpha^2 - 1.99/\alpha^3 & for\ \alpha \ge 1 \end{cases} \tag{2.1.5}$$

And for short edges clamped, the equations are as follows:

$$k_s = \begin{cases} 5.34/\alpha^2 + 2.31/\alpha - 8.39\cdot\alpha & for\ \alpha \le 1 \\ 5.34 + 2.31/\alpha - 3.44/\alpha^2 + 8.39/\alpha^3 & for\ \alpha \ge 1 \end{cases} \tag{2.1.6}$$

Curves for $\alpha \geq 1$ are plotted in Figure 10. Tension and compression stresses exist in the plate, equal in magnitude to the shear stress and inclined at 45°. The destabilizing influence of compressive stresses is resisted by tensile stresses in the perpendicular direction, often referred to as ‘tension field action’ in the literature. Unlike the case of edge compression, the buckling mode is composed of a combination of several waveforms and this is part of the difficulty in the buckling analysis for shear.

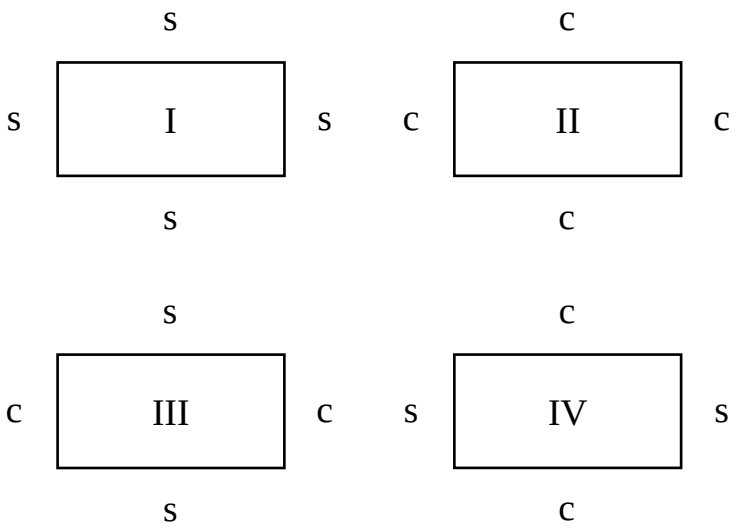

Figure 9 – Four Common Types of Edge Support

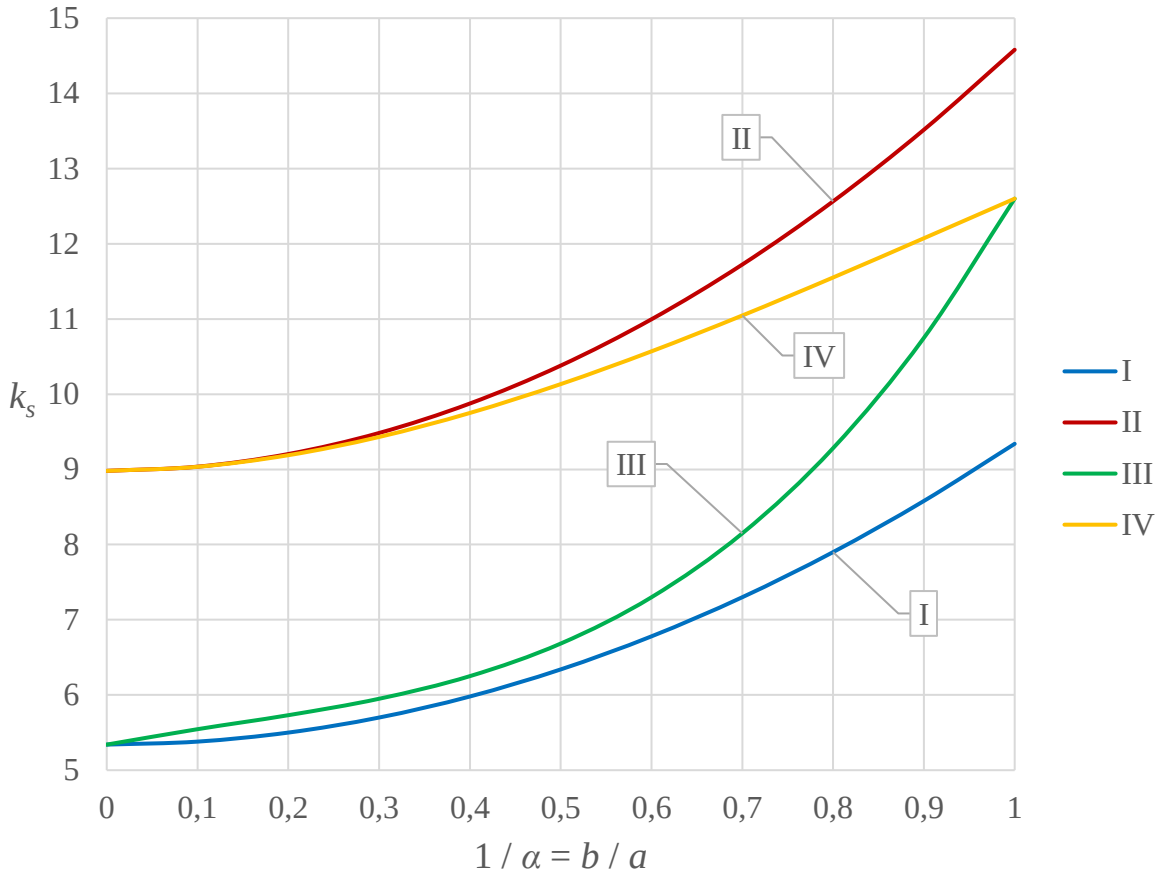

Figure 10 – Shear Stability Coefficients

Note: Figure 10 curves are engineering curves, which do not represent the actual nature of the buckling behavior, rather, provide an accurate and conservative estimate of the buckling coefficient. Nonetheless, values for infinitely long plate and square plate are exact. Asymmetric conditions edge support conditions are not included.

3.2 Geometry

For the purposes of this analysis, a square aspect ratio has been chosen. The general method presented may successfully be applied to various aspect ratios. The relative size of the cutout (its diameter) varies between 0.30 and 0.65 lengths of the side of the plate, which is a unit length (1 inch). The cutout is positioned in the center of the plate. For flanged holes, the flange thickness is equal to the plate thickness, which is 1% of the plate length. The flange is normal to the plane of the plate and its height is 5% of the cutout diameter. The pad-up thickness is 2% of the plate length or 200% of nominal plate thickness.

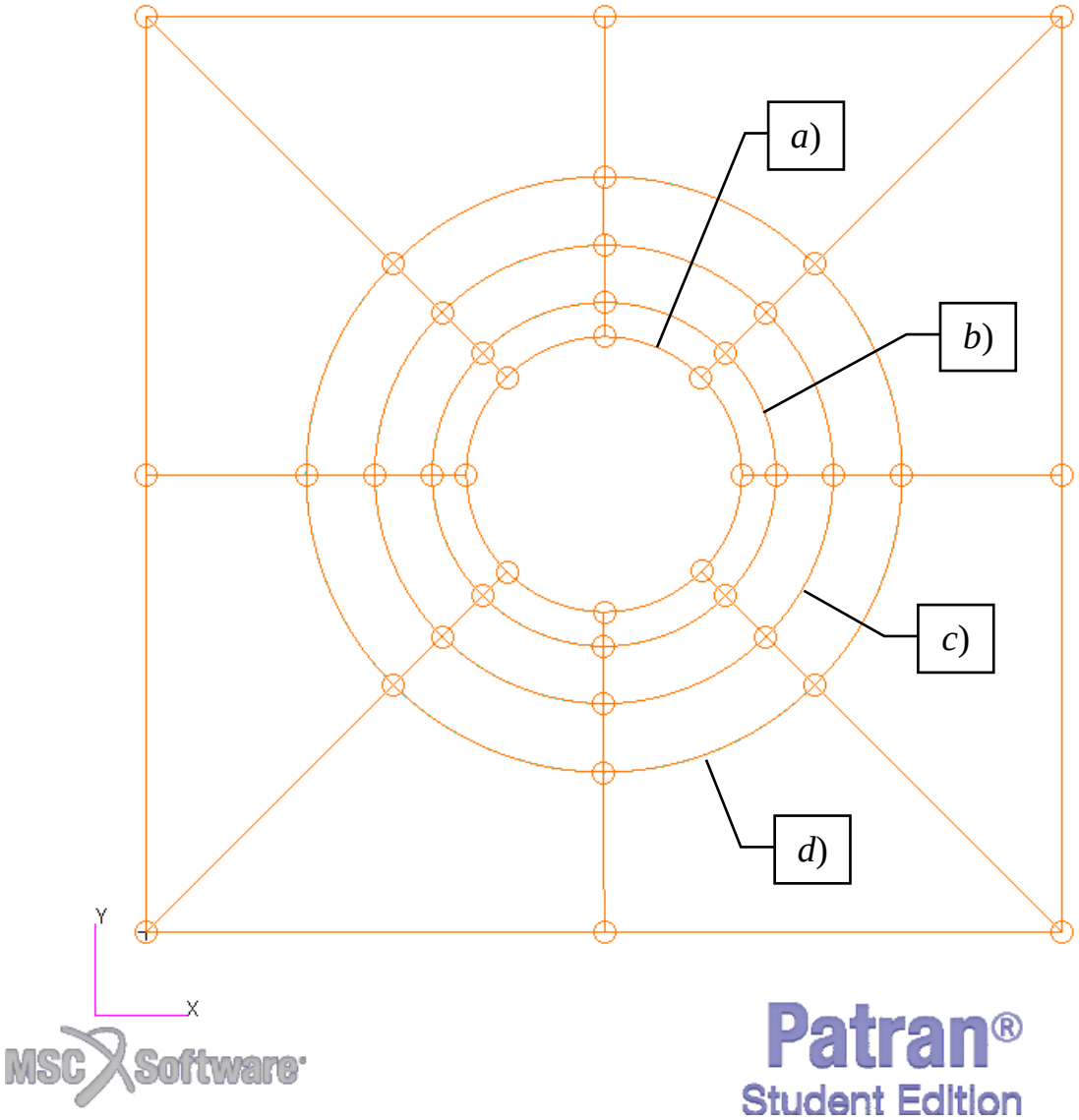

Figure 11 – Plate Geometry

For Plate Geometry, see Figure 11 on the previous page. Four configurations are depicted simultaneously: *a*) $d / b = 0.300$; *b*) $d / b = 0.375$; *c*) $d / b = 0.500$ and *d*) $d / b = 0.650$, where d is the hole diameter and b the length of the plate.

For Flange Geometry, see Figure 12 below.

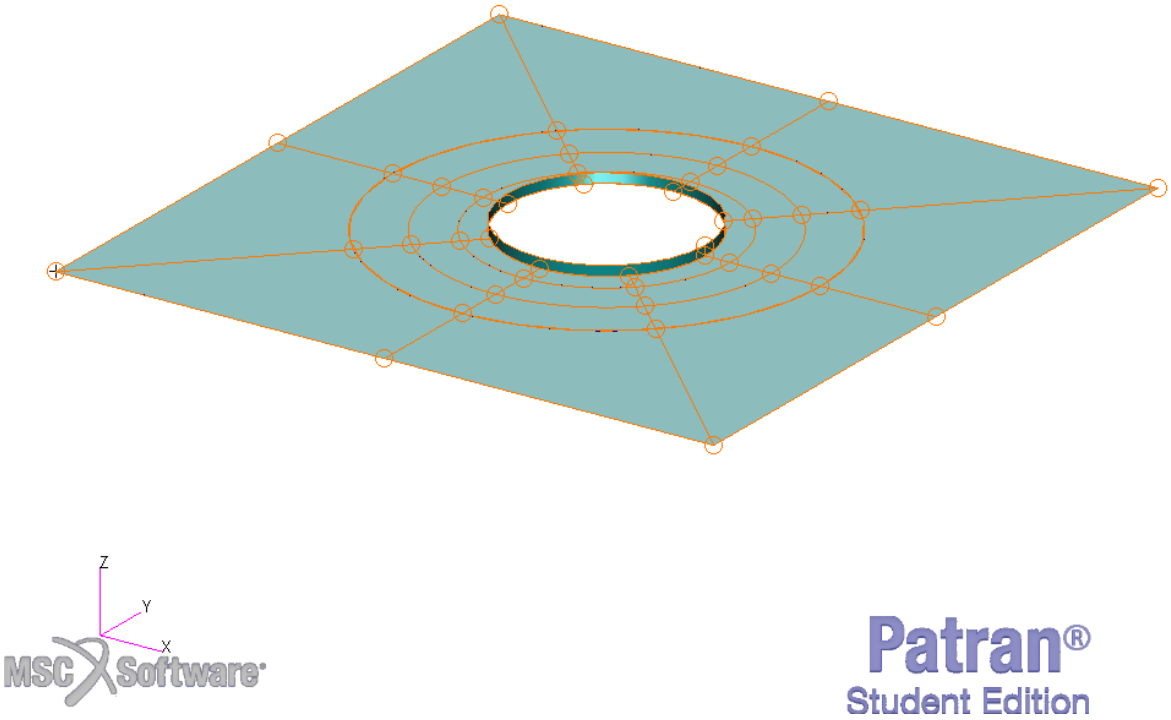

Figure 12 – Flange Geometry, $d / b = 0.300$, $a / b = 1.00$

3.3 Material Properties

The material properties are modelled after generic aluminum. The material is isotropic and linearly elastic.

$E = E_c = 10.00 \cdot 10^3$ ksi	Young's Modulus
$\nu = 0.33$	Poisson's Modulus
$G = \dfrac{E}{2(1+\nu)} = 3.759 \cdot 10^3$ ksi	Shear Modulus, implicitly defined
t = 0.01 in	Plate unpadded thickness

3.4 Mesh

Several meshes are built to establish the necessary limits for element size to maintain convergence of the results. Mesh is seeded with unidirectional length bias in certain locations. See Figure 13 for mesh seeds.

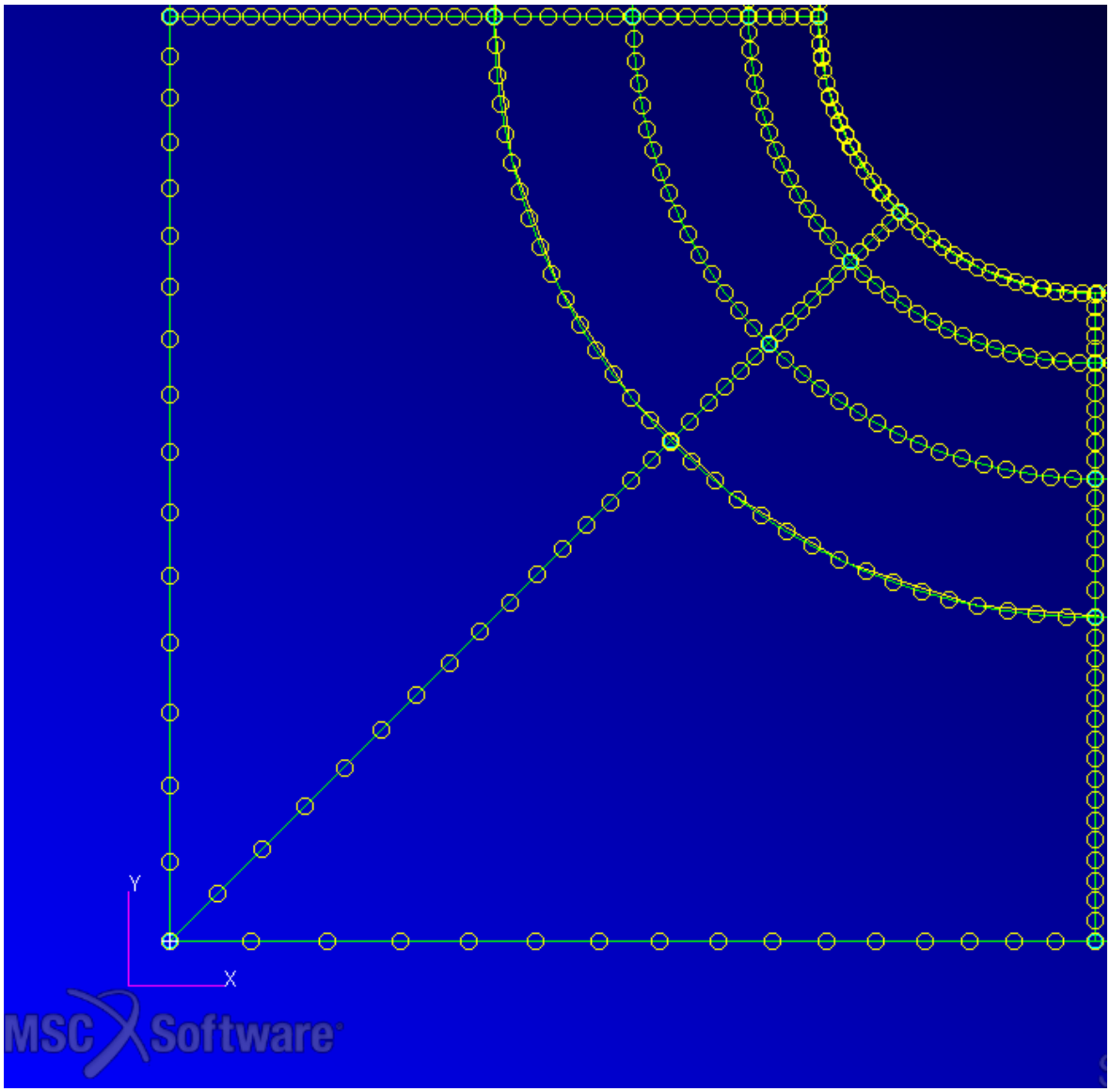

Figure 13 – Mesh Seeds (one quadrant shown)

By utilizing the geometric boundaries, the subregions are mappable with IsoMesh. Quadrilateral elements are chosen for mapping. For final mesh configuration, see Figure 14 below. Mesh verification is detailed later on.

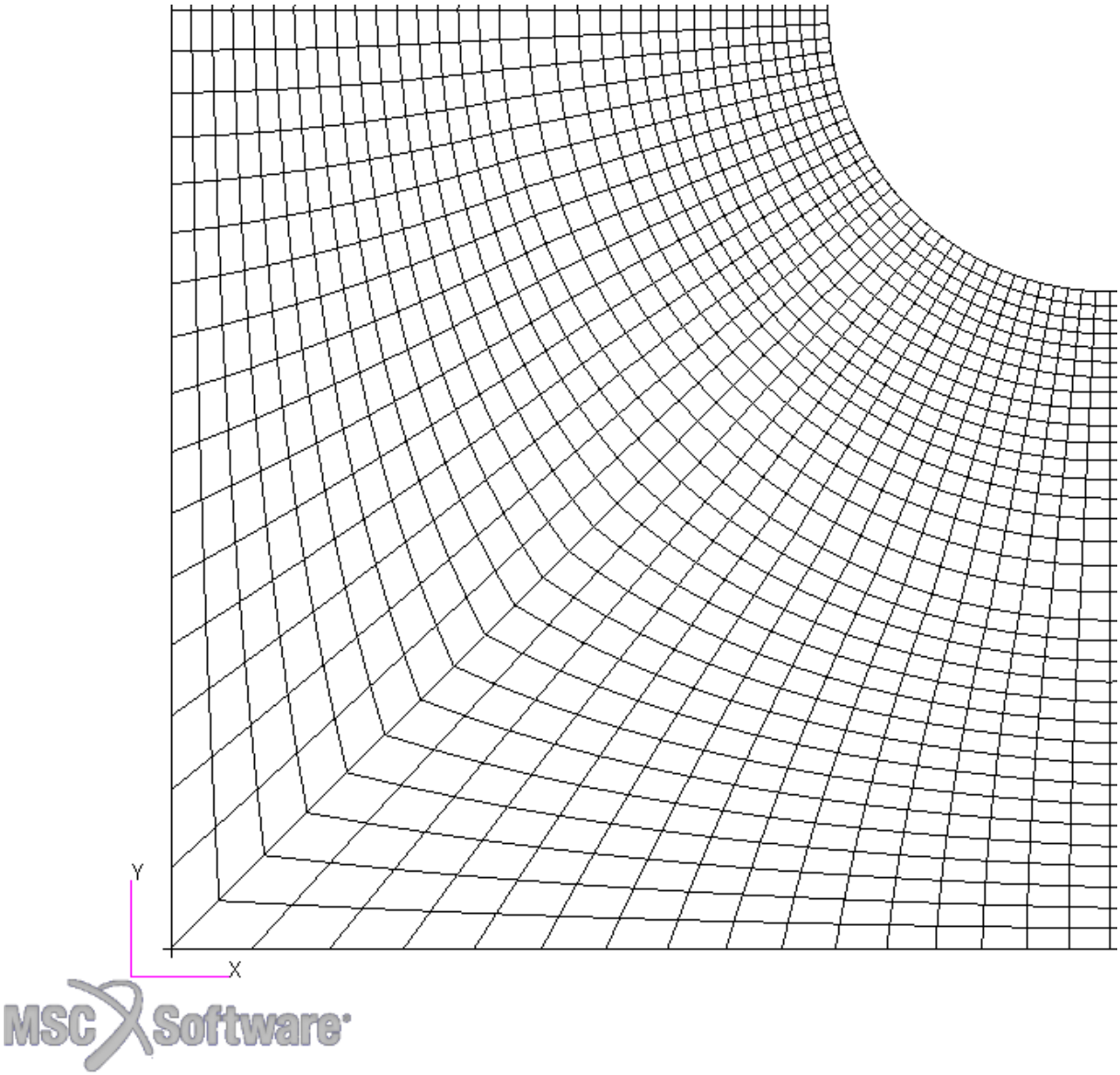

Figure 14 – Mesh Topology (one quadrant shown)

The mesh is symmetrical, which means all four quadrants are identical except for rotation by multiples of 90 degrees.

In order to obtain different hole sizes, the geometry around the cutout is simply deleted, i.e., meshes with different hole sizes are identical except for the region between the hole radii, which is removed for larger hole size.

See following pages for analysis of mesh quality.

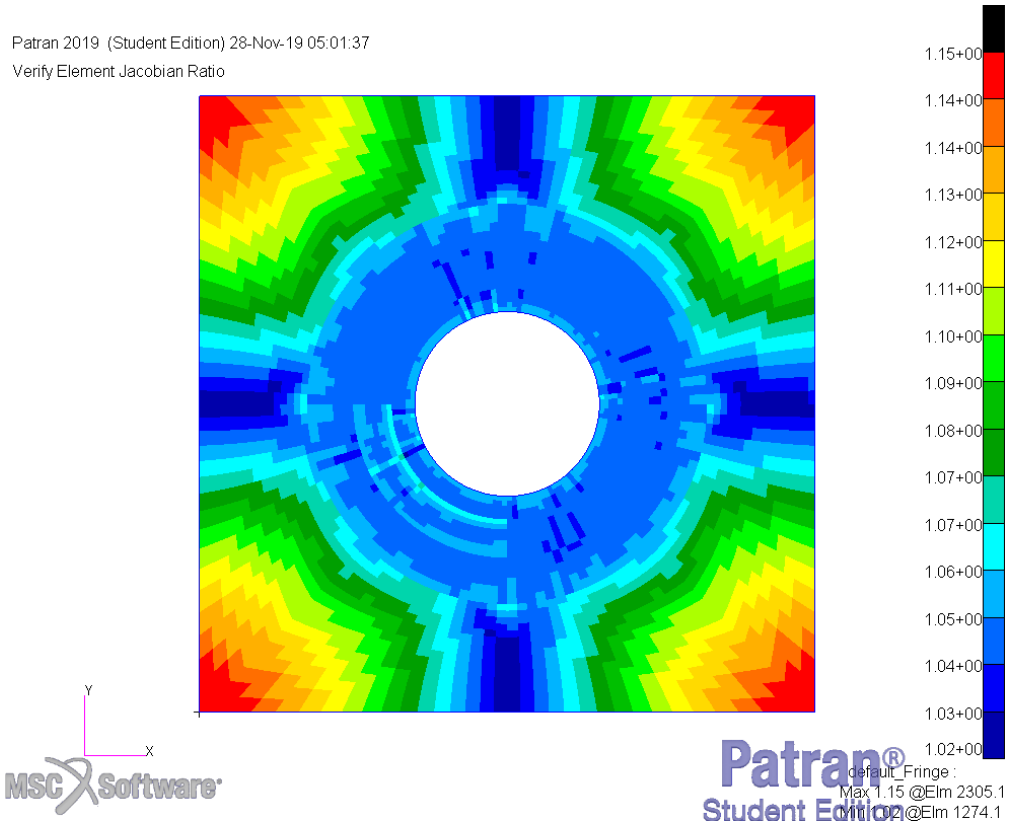

Figure 15 – Element Jacobian Ratio Verification

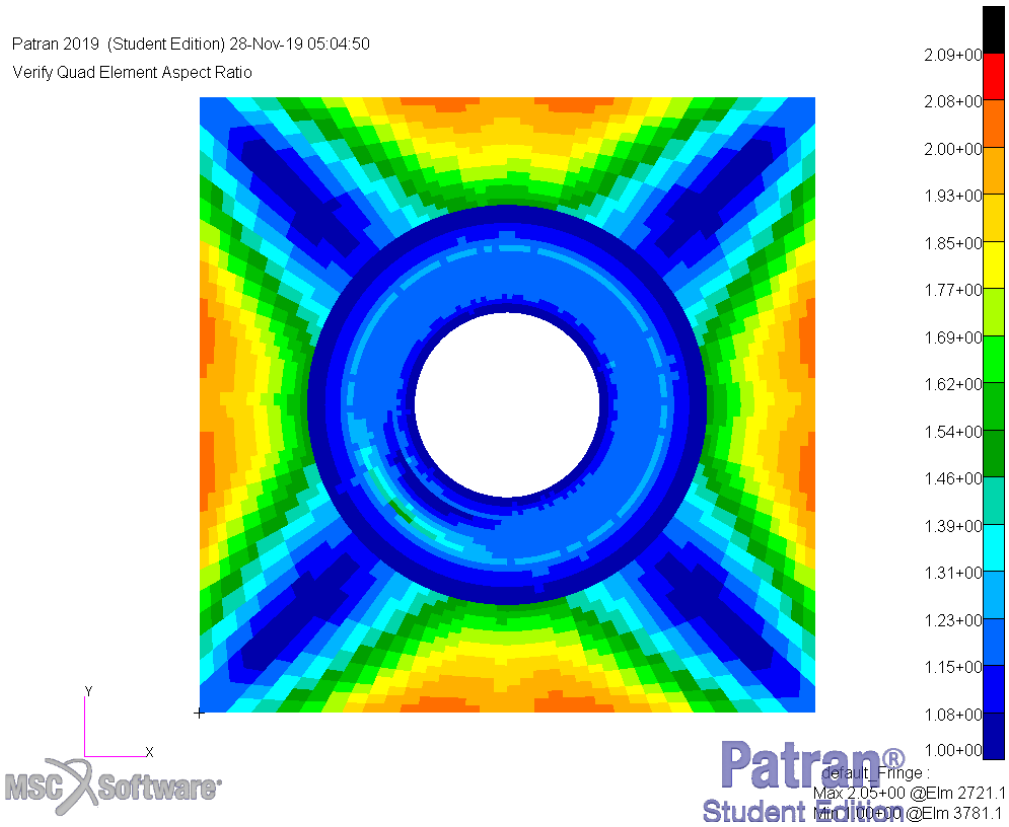

Figure 16 – Element Aspect Ratio

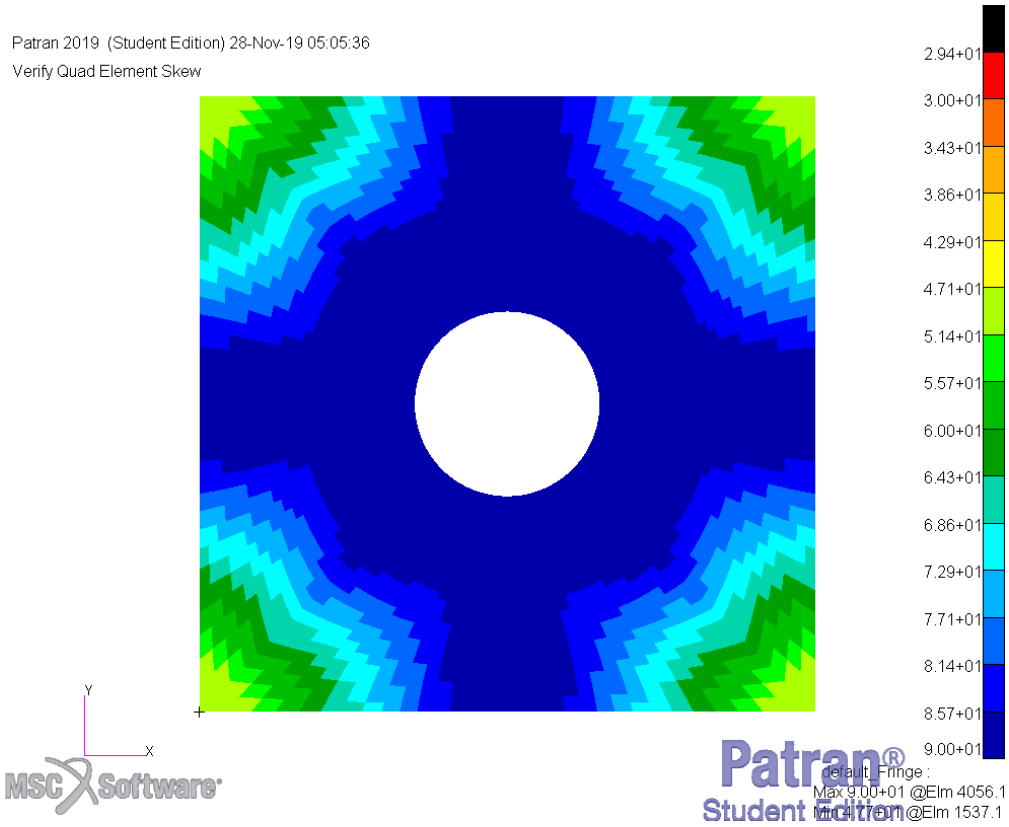

Figure 17 – Element Skew

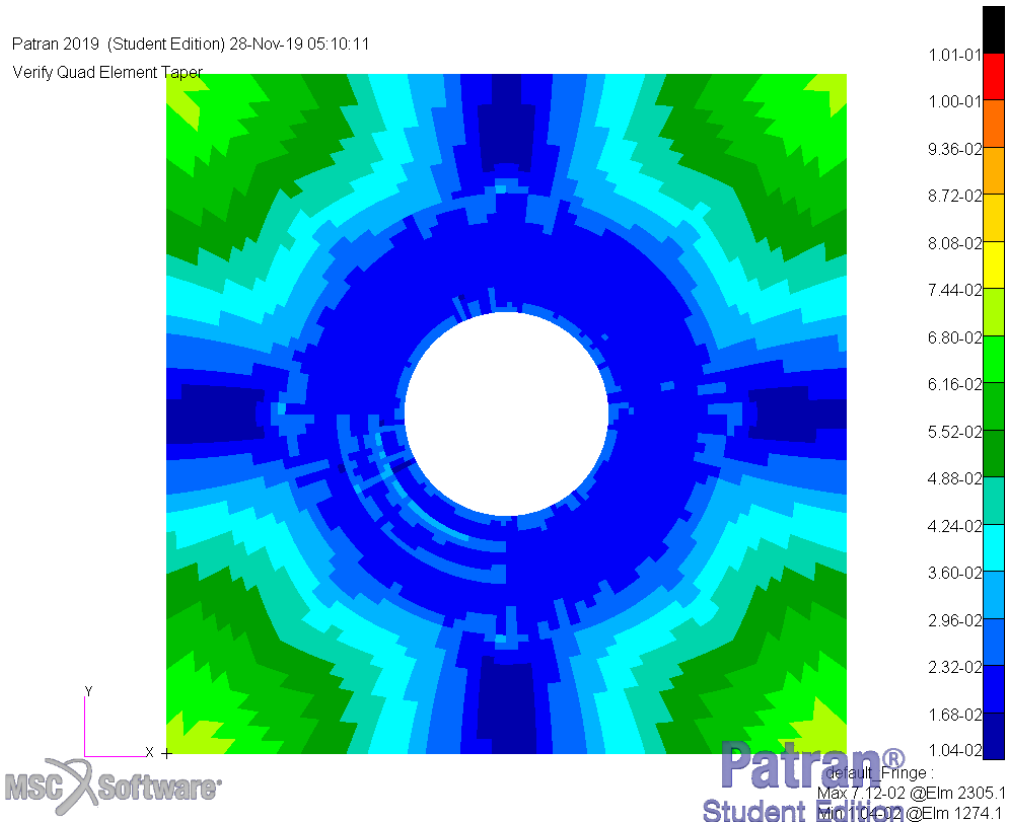

Figure 18 – Element Taper

Table 1 – Mesh Quality Parameters

Parameter	Max	Min
Jacobian Ratio	1.15	1.02
Aspect Ratio	1.00	2.09
Element Skew	90.0 deg	47.7 deg
Element Taper	0.0712	0.0104
Element Length	0.069 in	0.011 in

Mesh quality parameters are presented in Table 1. Overall, the mesh quality is deemed acceptable. The mesh is sufficiently refined to provide accurate results.

3.5 Boundary Conditions

The boundaries of the model are the edges of the hole or flange and the perimeter of the plate. Displacement constraints are used.

The boundary conditions are defined as follows for edges simply supported:

1) Edges of the hole or flange are free and unloaded.
2) The perimeter is constrained in translation along the Z axis (out of plane).
3) The corner (located at the origin) is constrained in any translation and rotation.

The boundary conditions are defined as follows for edges clamped:

1) Edges of the hole or flange are free and unloaded.
2) The perimeter is constrained in translation along the Z axis.
3) The perimeter is constrained in rotation about the vertical and horizontal axis.
4) The corner is constrained in any translation and rotation.

Thus, the model is sufficiently constrained.

3.6 Load Conditions

A uniform distributed unit shear is applied to the edges for pure shear. See Figure 19 below for positive shear sign convention.

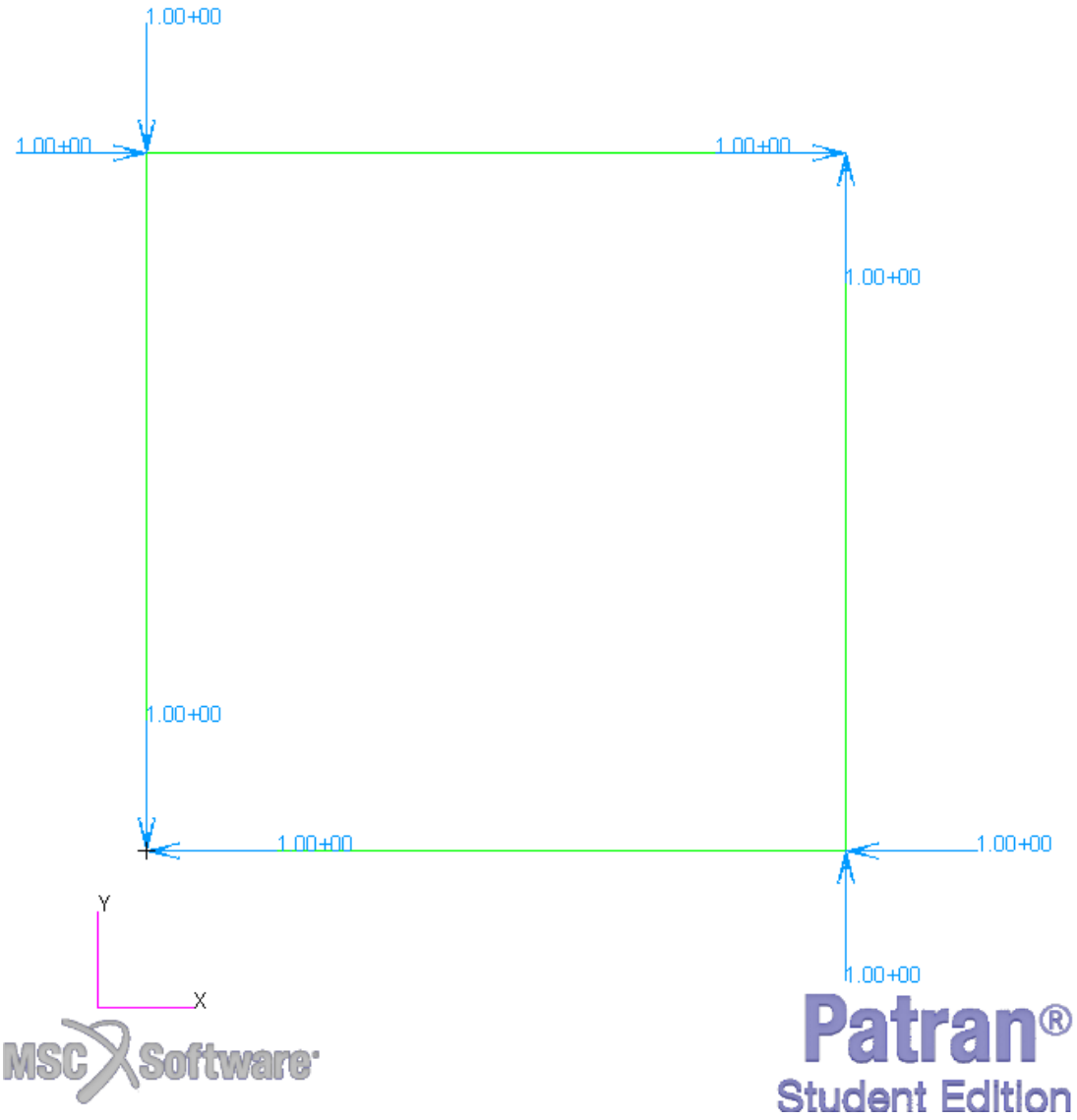

Figure 19 – Positive Uniform Unit Shear

3.7 Mesh Verification

In order to determine if the level of mesh refinement is sufficient for convergence of the results with test data, a model of a plate without a cutout is tested with various mesh sizes.

Table 2 – Mesh Convergence

n	N	ℓ, in	Simply Supported		Clamped	
			Fs_{cr}, ksi	k_s	Fs_{cr}, ksi	k_s
4	16	0.2500	13.526	14.654	34.440	37.314
6	36	0.1667	10.157	11.004	18.563	20.112
8	64	0.1250	9.297	10.073	15.554	16.852
12	144	0.0833	8.799	9.533	14.038	15.209
16	256	0.0625	8.667	9.390	13.690	14.833
24	576	0.0417	8.595	9.312	13.531	14.660
32	1024	0.0313	8.574	9.290	13.494	14.620
48	2304	0.0208	8.559	9.273	13.473	14.597
64	4096	0.0156	8.552	9.266	13.466	14.590

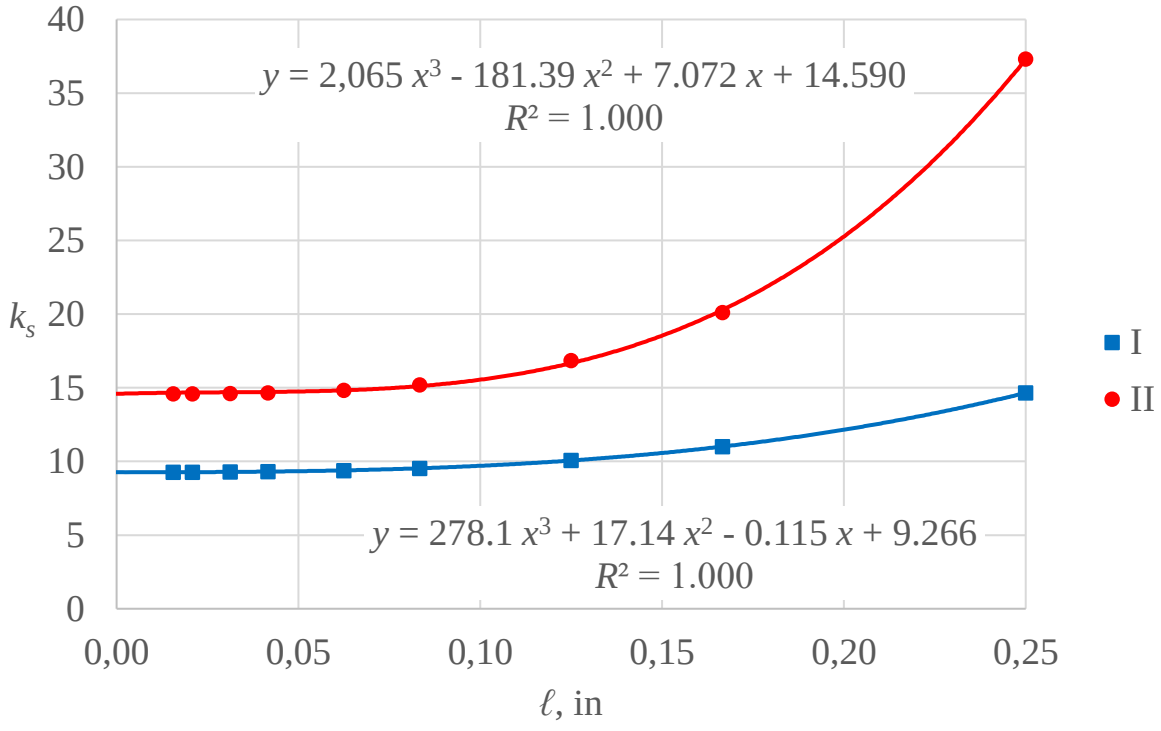

Figure 20 – Mesh Convergence

In Table 2, critical shear buckling stress Fs_{cr} is obtained directly from Patran solution by multiplying applied shear stress by the lowest positive eigenvector factor corresponding to the first buckling mode of the plate; n is the number of mesh elements along the length of the plate; N is the total number of elements (note, Patran license used allows up to 5,000 elements in a model) and k_s is obtained from the equation (3.1.2); ℓ is the length of the element. Note: I and II correspond to boundary conditions as described in Figure 9.

Example of calculations for $n = 64$, simply supported, is provided below.

$Factor = 85.52$

$b = 1$ in

$t = 0.01$ in

$P_s = 1$ lbs

$$f_s = P_s / (b \cdot t) = 1\,\text{lbs} / 0.01\,\text{in}^2 = 100\,\text{psi}$$

$$Fs_{cr} = f_s \cdot Factor = 100\,\text{psi} \cdot 85.52 = 8.552\,\text{ksi}$$

$$E = 10.00 \cdot 10^3\,\text{ksi}$$

$$\nu = 0.33$$

$$k_s = \frac{Fs_{cr} \cdot \left[12(1-\nu^2)(b/t)^2\right]}{\pi^2 E} = \frac{8.552\,\text{ksi} \cdot \left[12(1-0.33^2)(1\,\text{in}/0.01\,\text{in})^2\right]}{\pi^2 \cdot 10 \cdot 10^3\,\text{ksi}} = 9.266$$

Figure 20 is created by plotting k_s against ℓ from data contained in Table 2. It is observed that the mesh converges rapidly with increase in the number of elements, however, once the element length ℓ reaches 0.08 inches, increasing the mesh density provides diminishing returns.

Values of the shear coefficient obtained during mesh verification are very close to the theoretical values. The behavior of the plate resembles actual deformations observed in the physical experiments. The magnitude of translational eigenvectors is plotted in Figures 21 and 22 on the following page.

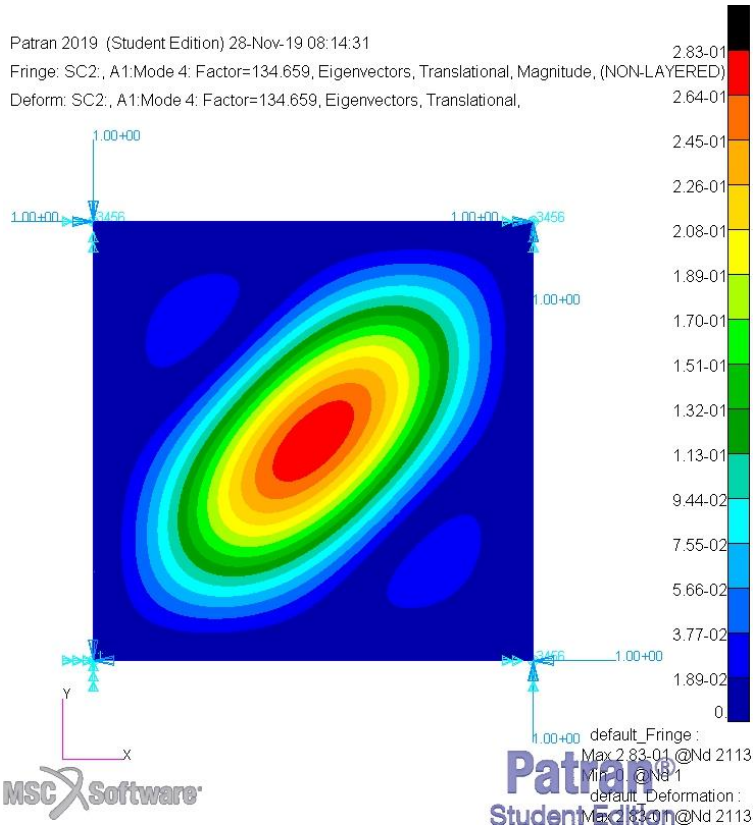

Figure 21 – Clamped Plate Buckling Mode

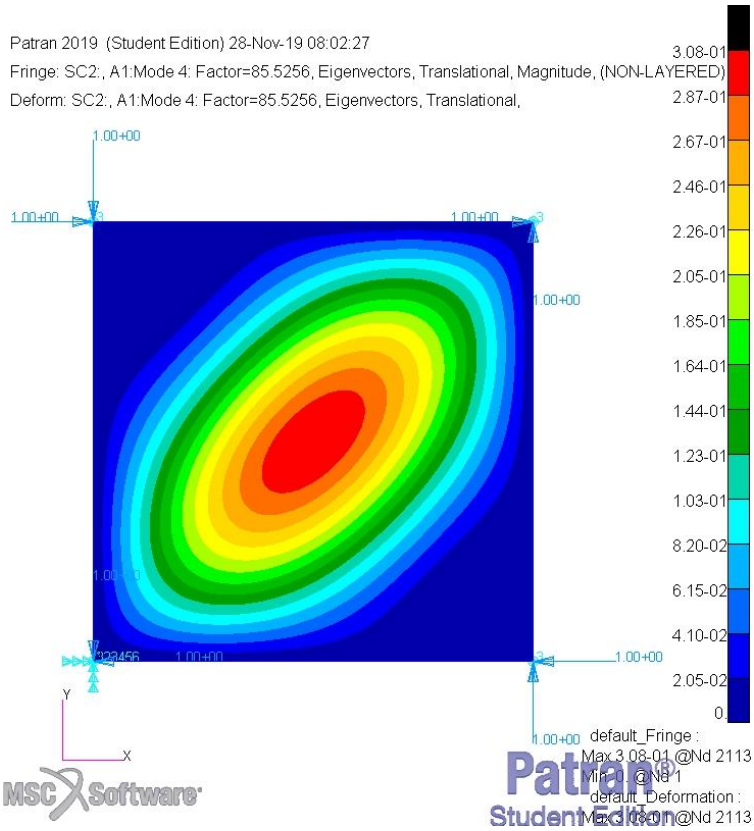

Figure 22 – Simply Supported Plate Buckling Mode

3.8 Effect of the Flange on Shear Buckling of a Plate with a Cutout

Buckling analysis is performed for a range of diameter to width ratios for both clamped and simply supported boundaries. Comparison between flanged hole and reference hole (without the flange) is made, according to Tables 3 and 4 below.

Table 3 – Plate Shear Buckling Stress

Fs_{cr}, ksi				
d / b	Clamped		Simply Supported	
	Flanged	Reference	Flanged	Reference
0.000	13.466	13.466	8.552	8.552
0.300	10.456	7.900	6.514	4.916
0.375	10.200	6.604	6.258	3.965
0.500	9.911	4.924	5.915	2.689
0.650	9.939	3.618	5.592	1.665

Table 4 – Plate Shear Buckling Coefficient

k_s				
d / b	Clamped		Simply Supported	
	Flanged	Reference	Flanged	Reference
0.000	14.59	14.59	9.266	9.266
0.300	11.33	8.56	7.06	5.33
0.375	11.05	7.16	6.78	4.30
0.500	10.74	5.34	6.41	2.91
0.650	10.77	3.92	6.06	1.80

Calculations in Tables 3 and 4 are calculated in the same was described during Mesh Verification. The gathered data is plotted in Figure 23. The relationships are approximated by polynomial equations. It is assumed that as the hole diameter approaches zero, the results should converge to correspond to the results of plate shear buckling without a cutout. Therefore, extrapolation is possible for smaller hole diameters.

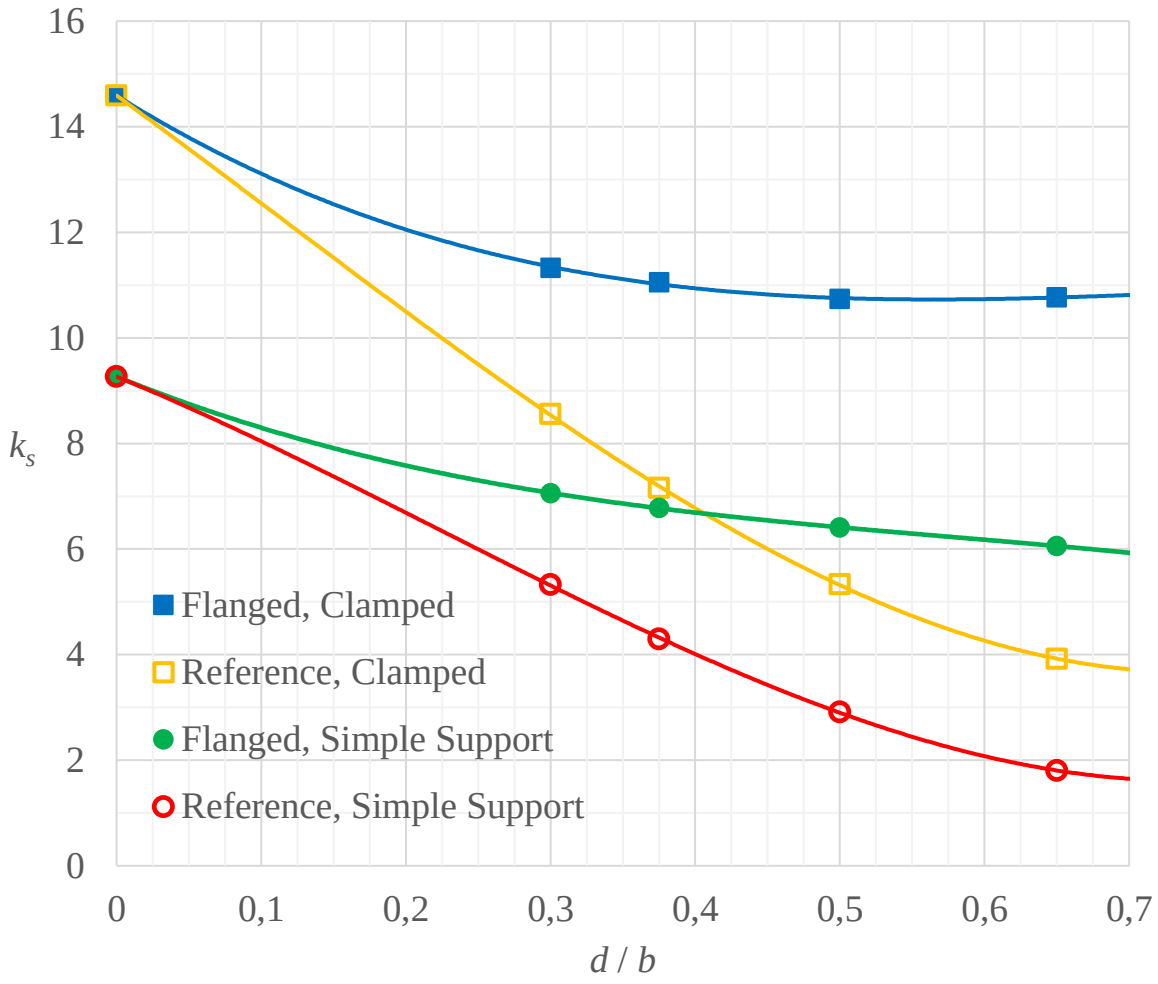

Figure 23 – Shear Buckling Coefficients Comparison

The best fit polynomials for Figure 23 above are as follows:

Table 5 – Polynomial Approximations

Series	Equation	R^2
Flanged, Clamped	$y = -10.77x^3 + 24.28x^2 - 17.12x + 14.59$	1.000
Flanged, Reference	$y = 17.45x^3 - 5.815x^2 - 20.00x + 14.59$	1.000
Flanged, Simple Support	$y = -8.719x^3 + 15.17x^2 - 11.11x + 9.266$	1.000
Reference, Simple Support	$y = 17.48x^3 - 11.71x^2 - 11.25x + 9.266$	1.000

3.9 Effect of the Flange on Stress Concentration in a Plate with a Cutout

For stress concentrations, no significant difference was observed between clamped and simply supported plates. The stress concentration results are therefore averaged. Comparison between flanged hole and reference hole (without the flange) is made, according to Tables 6 below.

Table 6 – Shear Stress Concentration

d / b	fs, psi		fs_{net}, psi
	Flanged	Reference	
0.000	100	100	100
0.300	247	265	143
0.375	289	308	160
0.500	381	417	200
0.650	574	651	286

Table 7 – Shear Stress Concentration Coefficients

d / b	Ks_g		Ks_{net}	
	Flanged	Reference	Flanged	Reference
0.300	2.47	2.65	1.90	2.04
0.375	2.89	3.08	1.99	2.12
0.500	3.81	4.17	2.10	2.29
0.650	5.74	6.51	2.21	2.51

where fs_{net} is the net shear stress, Ks_g and Ks_{net} are gross and net stress concentration coefficients respectively. These values are obtained as follows:

$$fs_{net} = \frac{P_s}{t \cdot (b - d)} = \frac{1\,\text{lbs}}{0.01\,\text{in} \cdot (1\,\text{in} - d)}$$

$$Ks_g = fs\,/\,100\,\text{lbs}$$

$$Ks_{net} = fs\,/\,fs_{net}$$

As seen from Table 6, peak shear stress is reduced if the hole is flanged. Maximum shear stress occurs in each quadrant of the plate.

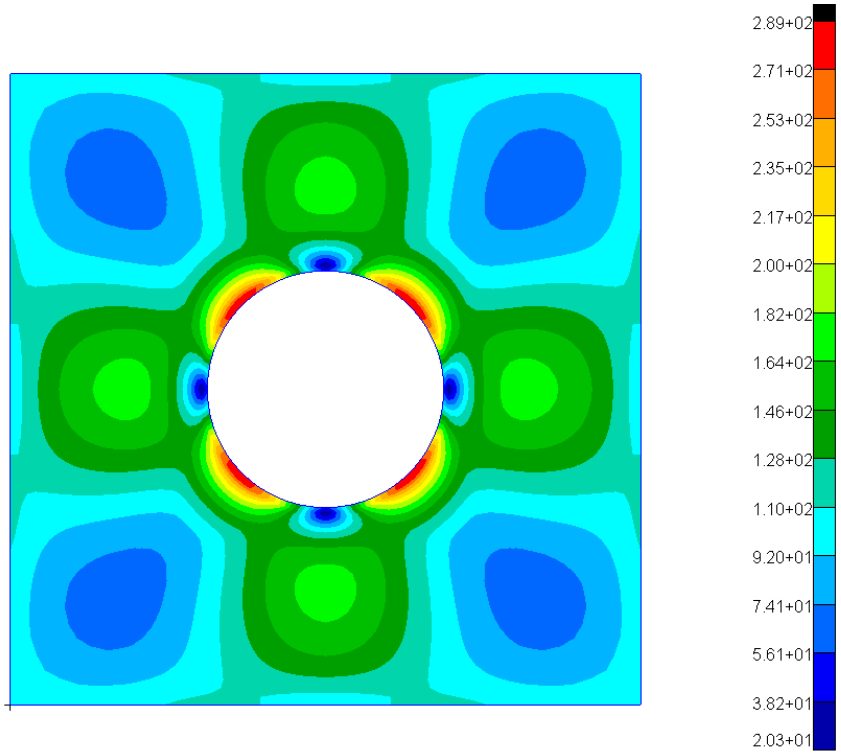

Figure 24 – Flanged Shear Stress Distribution, d / b = 0.375

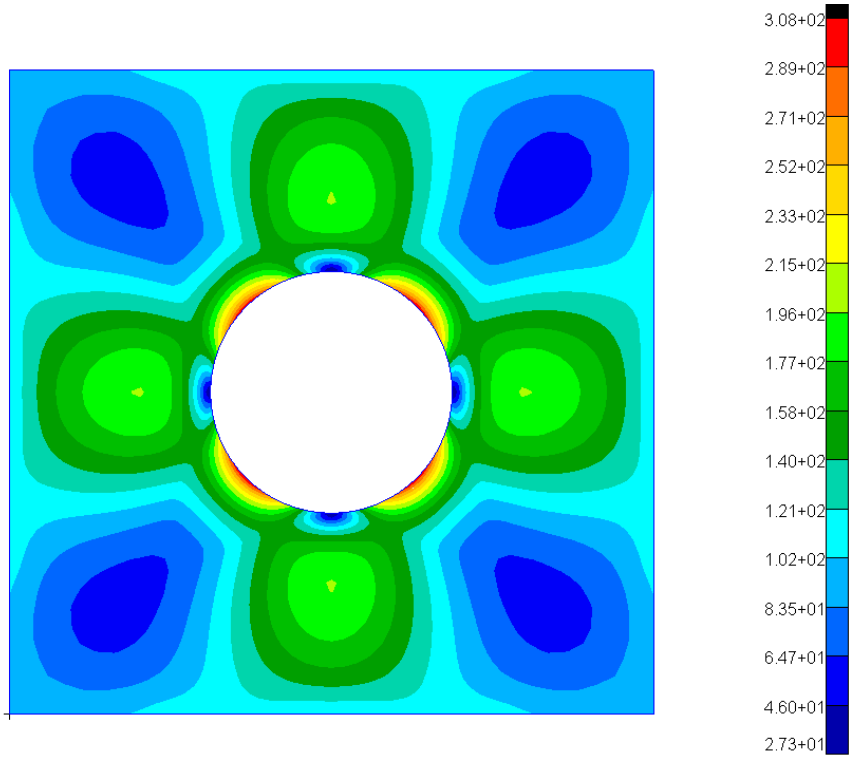

Figure 25 – Reference Shear Stress Distribution, d / b = 0.375

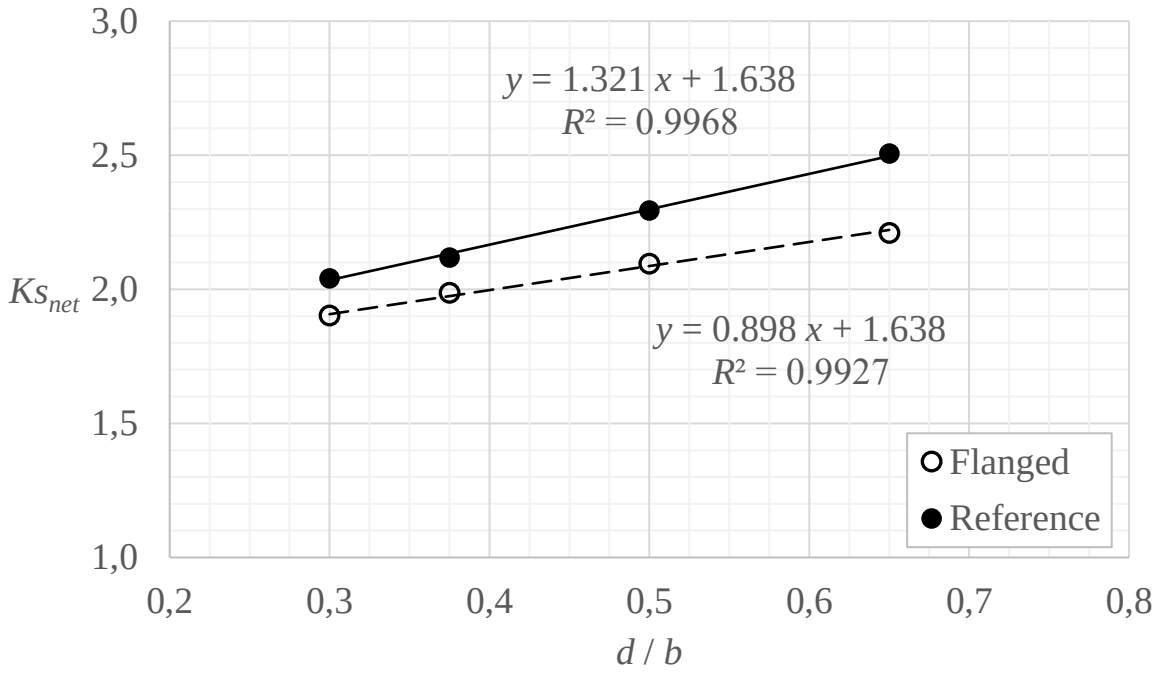

Figure 26 – Net Shear Stress Concentration

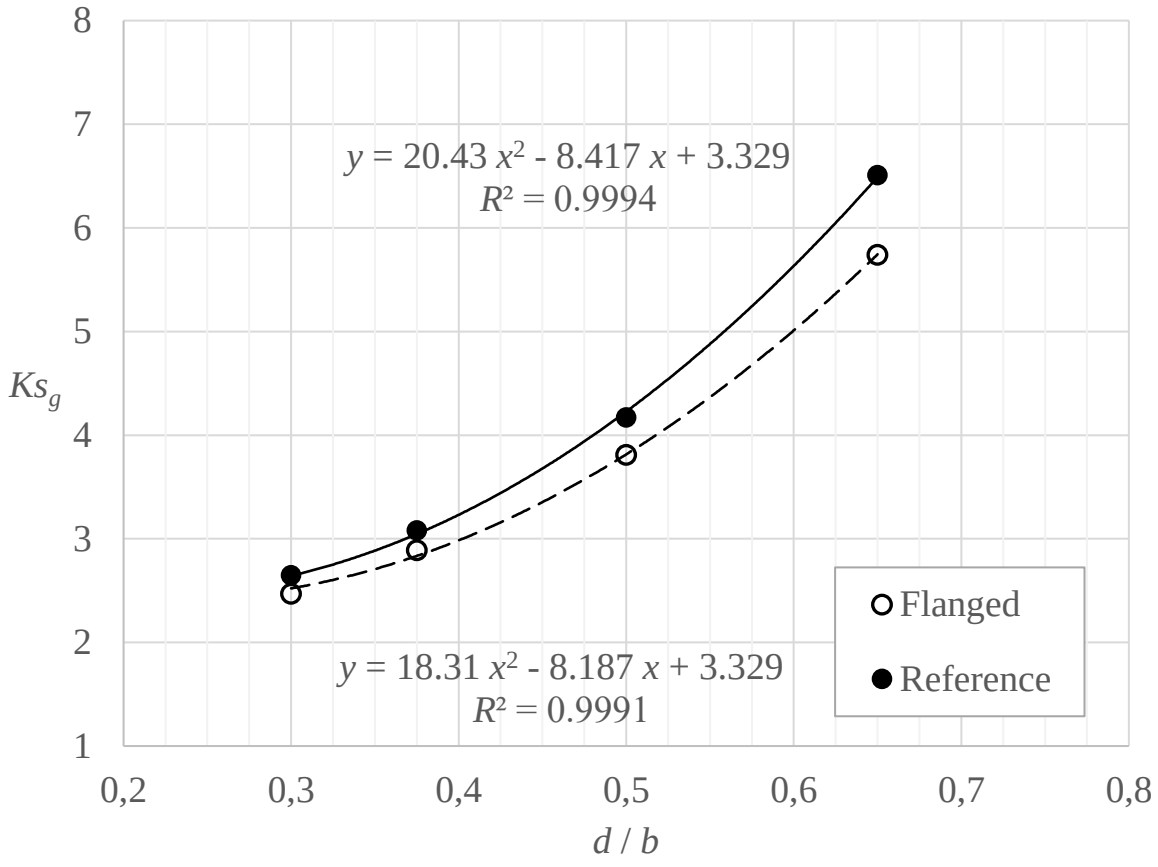

Figure 27 – Gross Shear Stress Concentration

From Table 6, shear stress concentration is plotted in Figures 26 and 27. It is observed that flanged hole has slightly lower shear stress concentration. The flange does not change the stress distribution significantly.

It should be noted that as d / b approaches zero, the difference between flanged and reference holes disappears.

3.10 Tensile Stress Distribution

Peak tensile stresses are obtained at the hole edge and are further illustrated in Figures 30 and 31 on the following pages. Also see Figures 28 and 29 for typical tensile stress distribution.

Table 8 – Peak Tensile Stresses

d / b	ft_{max}, psi		Kt_g		Kt_n		ft_{net}, psi
	Reference	Flanged	Reference	Flanged	Reference	Flanged	
0.000	100	100	not applicable				100
0.300	530	478	5.298	4.781	3.709	3.347	143
0.375	615	559	6.151	5.591	3.844	3.494	160
0.500	833	750	8.329	7.500	4.165	3.750	200
0.650	1297	1130	12.97	11.30	4.539	3.956	286

In Table 8, the following is assumed:

$$fs_{net} = f_{ref} \,/\, (1 - d / b)$$

$$Kt_g = ft_{max} / f_{ref}, \quad f_{ref} = 100 \text{ psi}$$

$$Kt_n = ft_{max} / ft_{net}$$

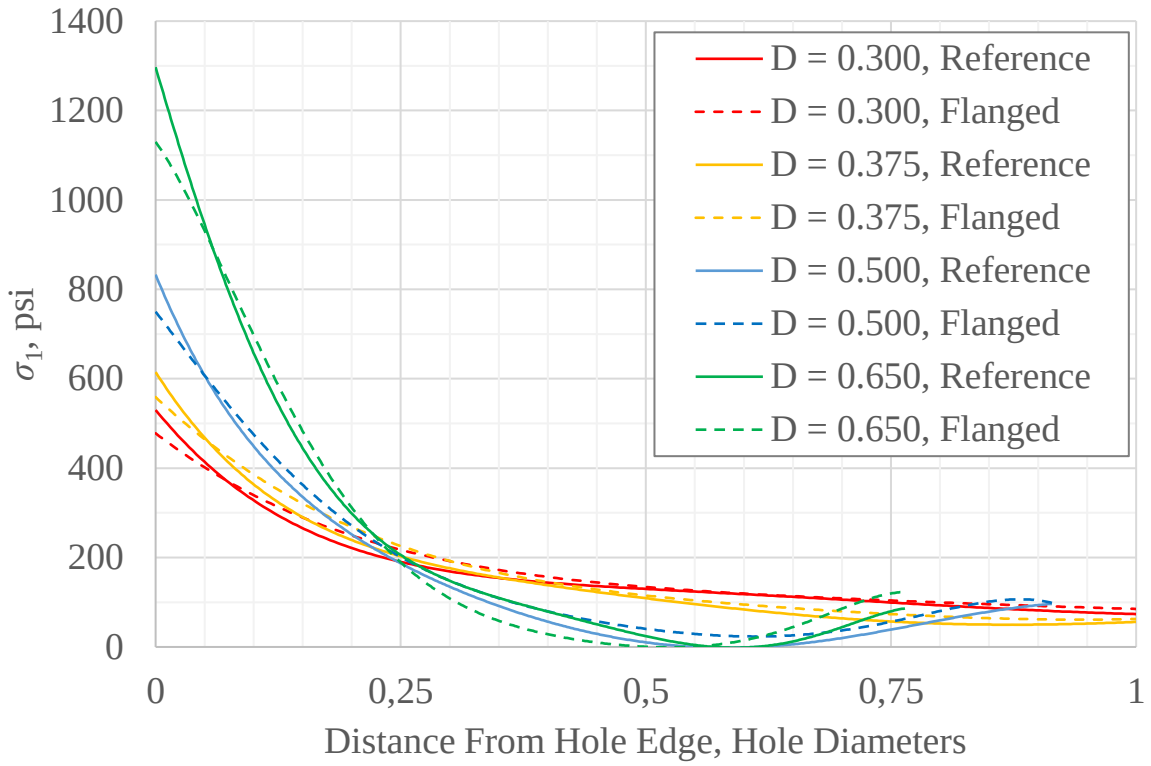

Figure 28 – Tensile Stress Concentration

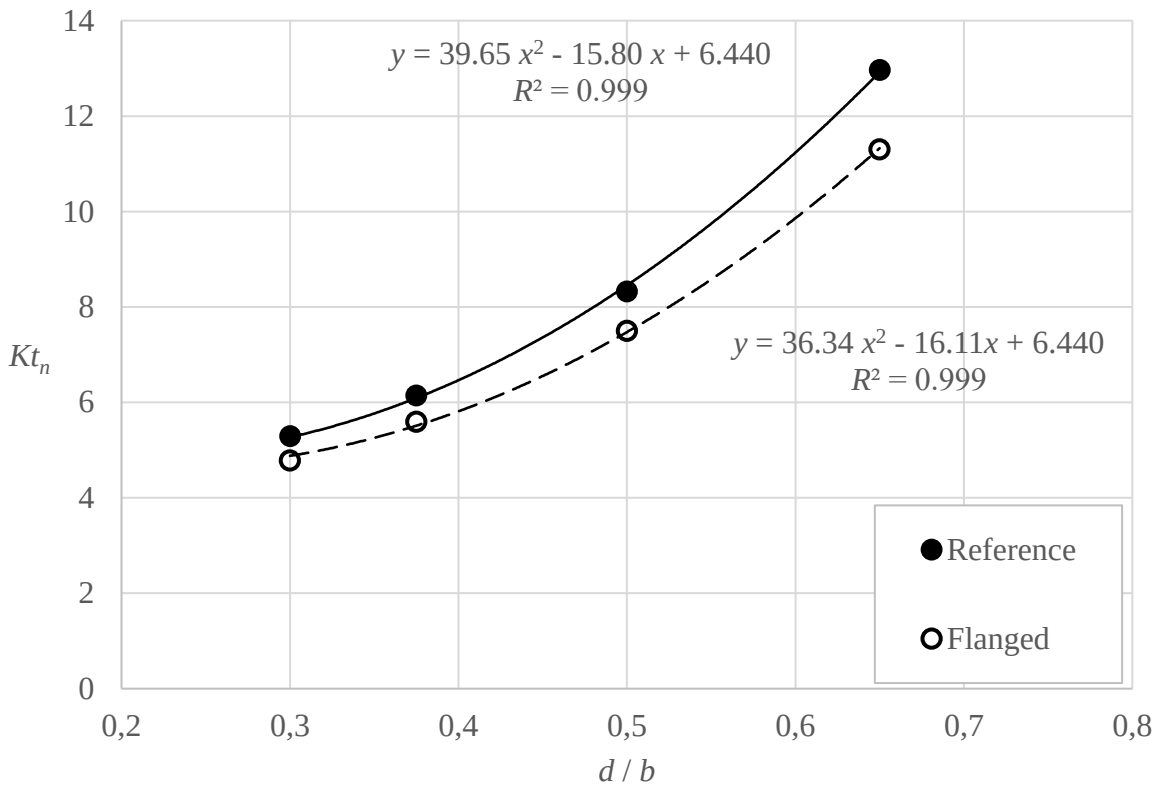

Figure 29 – Net Tensile Stress Concentration

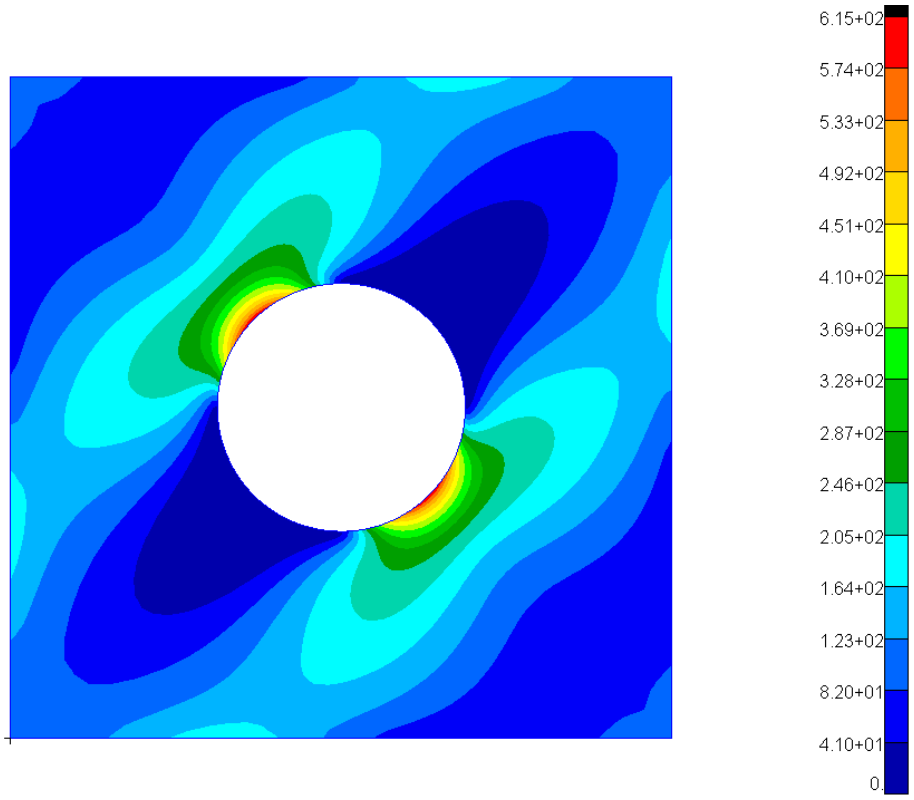

Figure 30 – Reference Diagonal Tension Field

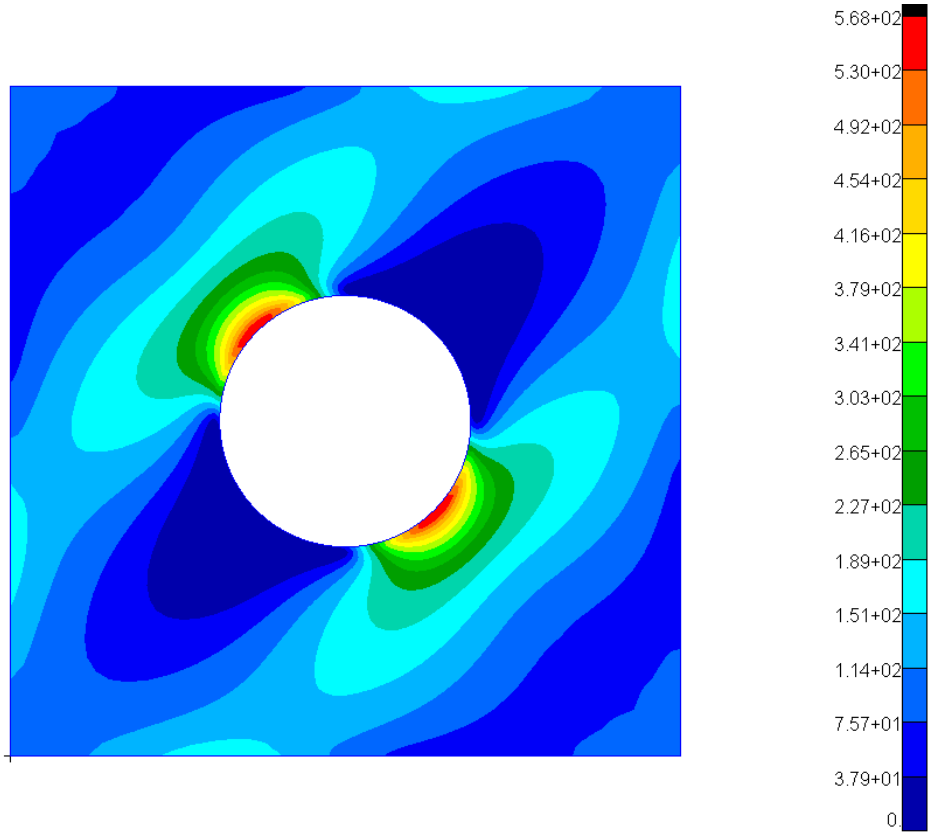

Figure 31 – Flanged Hole Diagonal Tension Field

3.11 Potential Weight Savings

Based on analysis performed, weight savings from utilizing cutout reinforcement may be calculated. Example calculation is performed for the following panel configuration:

- All edges simply supported,
- $a / b = 1.00$,
- $b / t = 100$. (reference)

$$Fs_{cr}\big|_{flanged} = Fs_{cr}\big|_{reference} \Rightarrow$$
$$\Rightarrow \left[k_s \cdot t^2\right]_{flanged} = \left[k_s \cdot t^2\right]_{reference} \Rightarrow$$
$$\Rightarrow \frac{[k_s]_{flanged}}{[k_s]_{reference}} = \left(\frac{t_{reference}}{t_{flanged}}\right)^2 = \left(\frac{6.78}{4.30}\right)^2 = (1.577)^2$$
$$t_{flanged} = t_{reference} / 1.577 = 63\% \cdot t_{reference}$$

In this case, the thickness of the plate may be reduced to 63% of original thickness without sacrificing the buckling capability. However, this may lead to net tension failure. Therefore, weight savings will ultimately be determined by shear or tension stress reduction, whichever is the smallest. However, more detailed analysis should always be performed for a specific panel configuration.

$$\frac{fs_{flanged}}{fs_{reference}} = \frac{289 \text{ psi}}{308 \text{ psi}} = 93.8\%$$
$$\frac{ft_{flanged}}{ft_{reference}} = \frac{559 \text{ psi}}{615 \text{ psi}} = 91.0\%$$

Stress obtained from Tables 6 and 8

The weight of the panel may be reduced to at least 93.8% of the original, assuming the weight of the flange is negligible, and the panel is not critical for buckling.

Discussion and Conclusions

There are potential limitations to gaining any benefit from reinforcement of cutouts by means of incorporating the flanged edge. Among those limitations, thicker materials usually require greater bend radii, which means that analysis geometry is not fully representative of the actual flange configuration. Additionally, it is usually not viable to make the flange normal to the plane of the plate. This is because of high residual tensile stresses resulting from the difference between the circumference of the formed flange edge and its initial flat pattern cutout. Residual tensile stresses are generally to be avoided in fatigue critical structure. Padding of the cutout perimeter is possible for thicker materials, furthermore, the flange may be machined (although the cost of such operation is probably substantial). This would allow for reduced stresses at the cutout perimeter, serve as a rigid platform for the flange and allow the use of full benefit of flange reinforcement.

Fillet between the plate and the flange needs to be incorporated to reduce further stress concentration. However, such a fillet is not necessary if the flange is cold formed. The fillet is unavoidable for machined flanges and may result in additional weight penalties.

Nonetheless, research shows that nearly all cutouts in structural members, such as frame or floor beam webs and ribs are reinforced in some way or another. If such a structure is to be analyzed, for example, when performing repairs, the effects of cutout reinforcement may be considered and benefited from.

References

1. Timoshenko, S. (1910), “Einge Stabilitätsprobleme der Elastizitätstheorie,” Z. Math. Phys., Vol. 58, pp. 337.
2. Timoshenko, S. (1934), “Stability of the Webs of Plate Girders,” Engineering, Vol. 138, p. 207.
3. Elgaaly, M. (1998). "Thin steel plate shear walls behavior and analysis." Thin-Walled Structures, 32(1-3), 151-180.
4. Libove, C., Ferdman, S., and Reusch, J. J. (1949). "Elastic buckling of a simply supported plate under a compressive stress that varies linearly in the direction of loading." NACA Technical Note No. 1891, 1891.
5. Papangelis, J. P., and Hancock, G. J. (1995). "Computer analysis of thin-walled structural members." Computers and Structures, 56(1), 157-176.
6. Peköz, T. (1987). "Development of a Unified Approach to the Design of Coldformed Steel Members." American Iron and Steel Institute.
7. Schafer, B. W. (2002). "Local, distortional, and Euler buckling of thin-walled columns." Journal of Structural Engineering, 128(3), 289-299.
8. Bryan, G. H. (1891), “On the Stability of a Plane Plate Under Thrusts in Its Own Plane, with Applications to the ‘Buckling’ of the Sides of a Ship,” Proc. London Math. Soc., Vol. 22.
9. Allen, H. G., and Bulson, P. S. (1980), Background to Buckling, McGraw-Hill, Maidenhead, Berkshire, England.
10. Compression After Exceeding the Buckling Load,” NLL-TR S-539. Bergman, S., and Reissner, H. (1932), “Über die Knickung von rechteckigen Platten beiSchubbeanspruchung,” Z. Flugtech Motorluftschiffahrt, Vol. 23, p. 6.
11. Seydel, E. (1933), Über das Ausbeulen von rechteckigen isotropen oder orthogonalanisotropen Platten bei Schubbeanspruchung,” Ing. Arch., Vol. 4, p. 169.

12. Moheit, W. (1939), “Schubbeulung rechteckiger Platten mit eingespannten Rändern,” Thesis, Technische Hochschule Darmstadt, Leipzig, Germany.
13. Iguchi, S. (1938), “Die Kninckung der rechteckigen Platte durch Schubkräfte,” Ing. Arch., Vol. 9, p. 1. Inoue, T., and Kato, B. (1993), “Analysis of Plastic Buckling of Steel Plates,” Int. J. Solids Struct., Vol. 30, No. 6, pp. 835–856.
14. Legget, D. M. A. (1941), “The Buckling of a Square Panel in Shear When One Pair of Opposite Edges Is Clamped and the Other Pair Simply Supported,” Tech. Rep. R&M No. 1991, British Aeronautical Research Council, London.
15. Rockey, K. C. (1980), “The Buckling and Post-buckling Behavior of Shear Panels Which Have a Central Circular Cut Out,” in Thin Walled Structures (ed. J. Rhodes and A. C. Walker), Granada, London.